IMAGE: A MAP OF THE STARS OF THE ORION CONSTELLATION

JournalPreview

London Journal of Engineering Research

Volume 24 | Issue 4 | Compilation 1.0

Great Britain Journals Press

WWW.JOURNALSPRESS.COM

JournalPreview

LONDON JOURNAL ENGINEERING RESEARCH

Journal Content
In this Issue

Great Britain Journals Press

Scan to know paper details and author's profile

Pulsed Electric Field Equipment for Electropastaurization of Dairy Products

Charles A. Duvoisin, José C. Tremarin, Sandra Duvoisin & Diogo J. Horst

INTRODUCTION

More than 549 million metric tons of cow's milk were produced in the world in 2023, and the production volume of cheese and butter exceeded 22 million tons, respectively. This is why food security in this sector is crucial.

To ensure that production is of high quality, Brazilian researchers developed industrial pasteurizing equipment that works with electrical fields. The invention is protected under patent WO2018090110 - system and method for neutralizing pesticides or similar agents contained in food and constructive configuration for its implementation.

Consumers are showing interest in preservation technologies that do not rely on heating. The effect of the device on the elimination of pathogens in dairy products is investigated.

Keywords: NA

Classification: DDC Code: 664.02

Language: English

Great Britain Journals Press

LJP Copyright ID: 392951
Print ISSN: 2631-8474
Online ISSN: 2631-8482

London Journal of Engineering Research

Volume 24 | Issue 4 | Compilation 1.0

Pulsed Electric Field Equipment for Electropastaurization of Dairy Products

Charles A. Duvoisin[α], José C. Tremarin[σ], Sandra Duvoisin[ρ] & Diogo J. Horst[Ↄ]

Author α σ ρ Ↄ: Brazilian Institute of Sciences and Innovations.

INTRODUCTION

More than 549 million metric tons of cow's milk were produced in the world in 2023, and the production volume of cheese and butter exceeded 22 million tons, respectively. This is why food security in this sector is crucial.

To ensure that production is of high quality, Brazilian researchers developed industrial pasteurizing equipment that works with electrical fields. The invention is protected under patent WO2018090110 - system and method for neutralizing pesticides or similar agents contained in food and constructive configuration for its implementation.

Consumers are showing interest in preservation technologies that do not rely on heating. The effect of the device on the elimination of pathogens in dairy products is investigated.

In addition to standardization, the industrial production of traditional cheeses seeks to guarantee safety, minimizing contamination and the survival of undesirable microorganisms, particularly pathogenic ones.

It should not be forgotten that complex and often unpredictable microflora dynamics are responsible for important organoleptic issues among cheeses. The ideal equalized modulation of the pulsed electric field avoids affecting the proteins and organoleptic properties of the milk, which can preserve the sensory properties of the cheese. Mastery of this technology is vital to maintain these properties with quality and nutritional security.

Treatment with pulsed electric fields is an emerging technology that has gained great importance in the dairy industry as a pre-treatment technique in the pasteurization process, enhancing the inactivation of microorganisms and enzymes at temperatures lower than those used in typical thermal treatments, such as those of ultra-high temperature. Our food processing technology uses short pulses of high-voltage electricity to selectively damage microbial and plant cell membranes.

The electric field is applied at room temperature for a short period of time (in the range of microseconds) causing a potential difference across the cell membrane, inducing a marked increase in membrane conductivity and permeability and affecting cell viability. greater amounts of certain heat-sensitive nutrients, such as vitamins, proteins and other compounds, necessary to preserve and enhance the flavor of foods, including cheese, milk, juices and packaged foods in general.

The challenges of using pulsed electric fields in food electropasteurization are addressed. Furthermore, the use of the technique in the valorization processes of cheese derivatives is discussed with the aim of promoting durable agri-food systems.

The equipment proves the complete sterilization of *salmonella* and other anaerobic bacteria including gram positive and gram negative. More information about this technology can be accessed at Duvoisin et al;. (2022).

REFERENCES

1. DUVOISIN, C.A.; HORST, D.J.; VIEIRA, R.A.; BARETTA, D.; PSCHEIDT, A.; SECCHI, M.A.;

London Journal of Engineering Research

ANDRADE JÚNIOR, P.P.; LANNES, SCS. Finite element simulation and practical tests on Pulsed Electric Field (PEF) for packaged food pasteurization: inactivating *E. coli, C. difficile, Salmonella spp.* and mesophilic bacteria. Food Science & Technology, 42, e115421, 2022. https://doi.org/10.1590/fst.115421.

2. DUVOISIN, C. A. (2017). WO2018090110 - System and method for neutralizing pesticides or similar agents contained in food and constructive configuration for its implementation. World Intellectual Property Organization. Retrieved from: https://patentscope.wipo.int/search/pt/detail.jsf?docId =WO2018090110.

Event-based Control Approach to Cyber-Security for Complex Discrete-Time Networked Systems

E Hassine, N. Gasmi, G. B. H Frej & A. Thabet

University of Gabes

ABSTRACT

Cyber-physical networks represent a new generation of complex networks whose normal functioning largely depends on the interactions between their physical and cybernetic components. Hence the importance of development and synthesis of approaches ensuring two essential tasks: Fault Detection and Isolation (FDI) and Fault Tolerant Attacks (FTA). It is in this context this paper is explored by proposing an observer-based FTA strategy to solve the problem of security in complex discrete-time systems. In fact, the synthesis of observers under conditions of convergence, stability, and robustness offers the possibility of reconstruction of the nodes-states, and to deduce a compensatory control law ensuring the stabilization of the global system. The synthesis method is based on the Lyapunov theory as well as the resolution of optimization problems in the form of Bilineair Matrix Inequality (BMI) with a switching condition for the implementation of the control gains. The theoretical results are validated by simulations on a 3-tanks system model.

Keywords: cyber-physical networks, FDI, FTA, control, BMI.

Classification: DCC Code: 005.8

Language: English

Great Britain
Journals Press

LJP Copyright ID: 392952
Print ISSN: 2631-8474
Online ISSN: 2631-8482

London Journal of Engineering Research

Volume 24 | Issue 4 | Compilation 1.0

Event-based Control Approach to Cyber-Security for Complex Discrete-time Networked Systems

E Hassine[α], N. Gasmi[σ], G. B. H Frej[ρ] & A. Thabet[ↀ]

ABSTRACT

Cyber-physical networks represent a new generation of complex networks whose normal functioning largely depends on the interactions between their physical and cybernetic components. Hence the importance of development and synthesis of approaches ensuring two essential tasks: Fault Detection and Isolation (FDI) and Fault Tolerant Attacks (FTA).

It is in this context this paper is explored by proposing an observer-based FTA strategy to solve the problem of security in complex discrete-time systems. In fact, the synthesis of observers under conditions of convergence, stability, and robustness offers the possibility of reconstruction of the nodes-states, and to deduce a compensatory control law ensuring the stabilization of the global system. The synthesis method is based on the Lyapunov theory as well as the resolution of optimization problems in the form of Bilineair Matrix Inequality (BMI) with a switching condition for the implementation of the control gains. The theoretical results are validated by simulations on a 3-tanks system model.

Keywords: cyber-physical networks, FDI, FTA, control, BMI.

Author α ↀ: MACS Research Laboratory, University of Gabes, Tunisia.
σ: Laboratoire d' Informatique and Télécommunications, ECAM Rennes-Louis de Broglie, Campus de Ker Lann-Bruz, Rennes, France.
ρ: IMS Laboratory, CNRS UMR 5218, University of Bordeaux, France.

Graphical Abstract

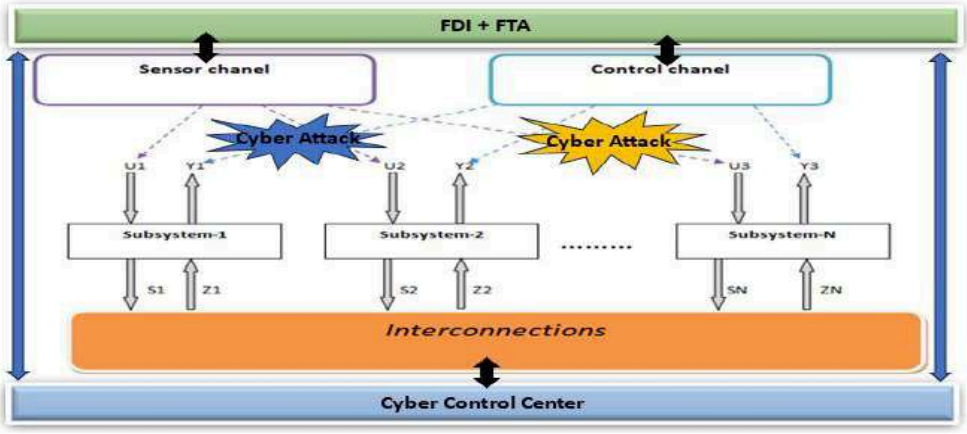

I. INTRODUCTION

Over the past two decades, the fields of mathematics, physics, computer science, and engineering have developed, enabling the proposal of alternative approaches to stabilizing and surveilling a large range of systems, including complex ones [1]-[2]. So, Control-supervision systems are becoming increasingly important and sophisticated from the point of view of the

communication network [3]-[4]. There is a growing need for safer methods and resilient systems, this has resulted in the development of fault-tolerant and attack-tolerant control systems [5]. In this context, it is essential to consider resilience in the FTA synthesis and what is manifested in the ability to maintain satisfactory levels of operation when conditions are unusual. Industrial supervision systems must take into account this essential property [6]. This is not the same as other information technology systems when data protection and related services play a major role in cybersecurity. Cyber-attacks on the Network Control System (NCS) can impact physical processes using the feedback principle. So, NCS security could benefit from a new approach based on control engineering methods [7], this research focuses on the study of how cyber-attacks are part of control algorithms, resulting in consequences for the physical part [8]. This field of research concentrates on the mathematical modeling of cyber-attacks and their effects on the physical process under control. Detecting cyber-attacks is possible by using dynamic models of physical processes and a control algorithm. Physical attacks and false data injection are the primary models taken into account when considering possible cyber-attacks on the NCS [9]. For instance, Various techniques have been explored and implemented to examine and evaluate these attacks, including graph theory in [10]. A secure set that has the potential for disturbance is what the maximum set of robustly controlled invariants is defined in [11]. In [12]-[13], the author emphasized the impact of cyber-attacks on all control inputs and all output measures of a disrupted system through an approach in the frequent domain.

Although the majority of work in this area is focused on approaches to complex continuous-time systems, little work has been done on complex discrete-time systems. The goal of this paper is to develop security measures using an observer-based feedback control for complex discrete-time systems. Model-based attack detection using observers is one of the components of this attack-tolerant control solution. A model-based approach is used in conjunction with classical fault-tolerant control to combine safety and security aspects in the proposed control. By utilizing a model of the dynamics system and available measurements, it compares the estimated output of the physical process [14]-[15]. If there is a discrepancy between the measurement and the fault-free model estimate, an appropriate control sequence will be created. For the purpose of attack and fault detection and isolation, we consider the design of an observer-based residual generator.

The present paper is introduced in the synthesis part of a new FTA approach and will be organized as follows: First, some useful preliminaries and a problem statement are presented. Secondly, an attack-tolerant controller is synthesized. Finally, numerical validation on an example will be presented. The last Section comprises some conclusions and future perspectives.

Notation: The following notation will be used throughout this paper:

- In a matrix, the notation (*) is used for the blocks induced by symmetry.
- $\bar{Q}^T$ is the transposed matrix of $\bar{Q}$; if $\bar{Q}$is a square matrix then the notation $\bar{Q} > 0$ ($\bar{Q} < 0$) means that $\bar{Q}$ is positive definite (negative definite).
- The set $Co(x, y) = \{\lambda x + (1 - \lambda)y, 0 \le \lambda \le 1\}$ is the convex hull of x, y.

II. PROBLEM STATEMENT AND PRELIMINARIES

In this section, we describe a modeling space for dealing with different types of attacks on control systems.

The physical system can be modelled by:

$$\begin{aligned} x_{k+1} &= Ax_k + B\tilde{u}_k + Ff_k \\ y_k &= Cx_k \end{aligned} \tag{1}$$

Where $x_k(t) \in R^{n_x}$ represent the sate vector, $y_k(t) \in R^{n_y}$is the output vector, $\tilde{u}_k \in R^{n_u}$ is the control vector, $f_k \in R^{n_f}$ is the unknown inputs represents the effect of faults,

London Journal of Engineering Research

$A = diag\{A_i\},\ B = diag\{B_i\}, C = diag\{C_i\},\ F = diag\{F_i\}$ designating constant matrices of appropriate dimensions.

For this type of system, we investigate a method of detection and identification of attacks based primarily on a model of detection and estimation of attack signals in two communication chains. For this, we propose to apply this form of Luenberger observer:

$$\begin{aligned} \hat{x}_k &= A\hat{x}_k + Bu_k + L(\tilde{y}_k - \hat{y}_k) \\ \hat{y}_k &= C\hat{x}_k \end{aligned} \tag{2}$$

The control signal, by principle of output feedback, is designed with the following form:

$$u_k = K_1\hat{y}_k + K_2\tilde{y}_k \tag{3}$$

The faults and attacks are modelled as follows:

- Physical attacks are like fault signals so f_k(, will be considered as physical attacks.
- Since data corruption / modification can change the control sequences and measurements provided by the different sensors from their actual calculations or values «u_k», «y_k» to corrupted signals «$\tilde{u}_k$» and «$\tilde{y}_k$».

False attacks are modelled by:

$$\begin{aligned} \tilde{u}_k &= u_k + \Gamma^u b_k^u \\ \tilde{y}_k &= y_k + \Gamma^y b_k^y \end{aligned} \tag{4}$$

With $b_k^u$and b_k^y represents the pirated data. Γ^u and $\Gamma^y$are the binary impact matrices indicating which data strings can be accessed by the "hacker".
Now we define a new variable α_k, group the fault/attack signals as follows: $\alpha_k = \left(f_k\ b_k^u\ b_k^y\right)^T$.

This allows us to rewrite the augmented system (system + observer) as follows:

$$\begin{aligned} \eta_{k+1} &= A_\alpha\eta_k + B_\alpha\alpha_k \\ y_\alpha &= C_\alpha\eta_k \end{aligned} \tag{5}$$

With

$$\eta_k = \begin{bmatrix} x_k \\ \hat{x}_k \end{bmatrix}, y_\alpha = \begin{bmatrix} y_k \\ \hat{y}_k \end{bmatrix}$$

$$A_\alpha = \begin{pmatrix} A + BK_2C & BK_1C \\ LC + BK_2C & A - LC + BK_1C \end{pmatrix}$$

$$B_\alpha = \begin{pmatrix} F & B\Gamma^u & BK_2\Gamma^y \\ 0 & 0 & (L + BK_2)\Gamma^y \end{pmatrix}, C_\alpha = \begin{pmatrix} C & 0 \\ 0 & C \end{pmatrix}$$

Then the following lemmas are considered:

Lemma 1 [16] Given two matrices X, Y, of appropriate dimensions, then the following inequality holds for any constant $\beta > 0$

$$X^TY + Y^TX \le \beta X^TX + \beta^{-1}Y^TY \tag{6}$$

Lemma 2 [16] Consider a nonlinear function $h: R^n \to R^n$, the following two items are equivalent:

- h is globally Lipschitz with respect to its argument, i.e.,

$$\| h(a) - h(b) \| \le l \ \| \ a - b \ \| \tag{7}$$

- there exist constants $h_{ij}$and $\bar{h}_{ij}$ so that for all $\forall a, b \in R$there exist $r_i \in Co(a, b)$, $r_i \neq a, r_i \neq b$ and functions $h_{ij}: R^n * R^n$ satisfying the following equality:

$$h(a) - h(b) = \sum_{i,j=1}^{q,n} h_{ij}\ (r_i) H_{ij}\ (a - b) \tag{8}$$

And $\underline{h}_{ij} \le h_{ij}(r_i) \le \bar{h}_{ij}$ where $h_{ij}(r_i) = \frac{\partial h_i}{\partial h_j}(r_i)$ and $H_{ij} = e_q(i)e_n^T(j)$

III. FTA SYNTHESIS

This section is dedicated to the development of the new FTA synthesis. The main result is given by the following Theorem:

Theorem 1 There exists an asymptotic stable observer of the form (2) and an event-based fault-attack tolerant controller (3), with a triggering condition $\| \alpha_k \|^2 \le \sigma \| \eta_k \|^2$, for the system (1), if there exists positive symmetric matrices

$P = \begin{pmatrix} P_1 & 0 \\ 0 & P_2 \end{pmatrix}$, matrices $R = P_2 L$, K_1, K_2 and a positive scalar β, solution if the following BMI is feasible:

$$\begin{pmatrix} A_\alpha^T P A_\alpha - P & A_\alpha^T P B_\alpha & 0 \\ * & (\beta^{-1} I)^{-1} & 0 \\ * & * & B_\alpha^T P B_\alpha + \sigma\beta I \end{pmatrix} < 0 \tag{9}$$

With

$$A_\alpha^T P A_\alpha - P = \begin{pmatrix} Q_{11} & Q_{12} \\ Q_{21} & Q_{22} \end{pmatrix}$$

$$Q_{11} = (A^T P_1 A + A^T Z C + C^T Z^T A + C^T W C + \mu C^T W C + \mu C^T$$
$$Y C + \mu C^T Y^T C + \mu C^T X C) - P_1 Q_{12} = A^T Z_1 C + C^T W_2{}^T C + \mu C^T Z^T A - \mu C^T Y C + \mu C^T W_2{}^T C$$
$$+ \mu C^T R^T A - \mu C^T X C + \mu C^T Y_1{}^T C Q_{21} = C^T Z_1{}^T A + C^T W_2 C + \mu A^T Z C + \mu A^T R C - \mu C^T Y^T C -$$
$$\mu C^T X C + \mu C^T W_2 C + \mu C^T Y_1 C Q_{22} = (C^T W_1 C + \mu A^T P_1 A - \mu A^T R C + \mu A^T Z_1 C - \mu C^T R^T A$$
$$+ \mu C^T X C - \mu C^T Y_1{}^T C + \mu C^T Z_1{}^T A - \mu C^T Y_1{}^T C + \mu C^T W_1 C)$$
$$- \mu P_1$$

$$A_\alpha^T P B_\alpha = \begin{bmatrix} A_{11} & A_{12} & A_{13} & A_{21} & A_{22} & A_{23} \end{bmatrix}$$

$$A_{11} = A^T P_1 F + C^T Z^T F, A_{12} = A^T P_1 B\Gamma^u + C^T Z^T B\Gamma^u A_{13} = A^T Z\Gamma^y + C^T W\Gamma^y + \mu C^T Y\Gamma^y + \mu C^T X\Gamma^y + \mu C^T Y^T\Gamma^y$$
$$A_{21} = C^T Z_1{}^T F, A_{22} = C^T Z_1{}^T B\Gamma^u, A_{23} = C^T W_2\Gamma^y ++ \mu A^T R$$
$$\Gamma^y + \mu A^T R\Gamma^y + \mu A^T Z\Gamma^y - \mu C^T X\Gamma^y - \mu C^T Y^T\Gamma^y + \mu C^T Y_1\Gamma^y + \mu C^T W_2\Gamma^y$$

$$B_\alpha^T P B_\alpha = \begin{bmatrix} F^T P_1 F & F^T P_1 B\Gamma^u & A^T Z\Gamma^y & * & \Gamma^{u^T} B^T P_1 B\Gamma^u & \Gamma^{u^T} B^T Z\Gamma^y & \Gamma^{y^T} Z^T F & \Gamma^{y^T} Z^T{}_1 B\Gamma^u & B_{33} \end{bmatrix}$$

$$B_{33} = \Gamma^{y^T} W\Gamma^u + \mu\Gamma^{y^T} X\Gamma^y + \mu\Gamma^{y^T} Y^T\Gamma^y + \mu\Gamma^{y^T} Y\Gamma^y$$

$$+ \mu\Gamma^{y^T} W\Gamma^y$$

and $L = \{\mu P_1\}^{-1} R;\ K_1 = B^+ P_1^{-1} Z_1; K_2 = B^+ P_1^{-1} Z.$

Proof

To determine the different control and observer gains, a stability analysis is based on the Lyapunov function:

$$\Delta V = V_{k+1} - V_k < 0 \tag{10}$$

With $V_k = \eta_k^T P \eta_k, V_{k+1} = \eta_{k+1}^T P \eta_{k+1}.$

Now using lemma 1 on «ΔV », the latter becomes:

London Journal of Engineering Research

$$\Delta V = \eta_k^T [A_\alpha^T P A_\alpha + \beta^{-1} A_\alpha^T P B_\alpha B_\alpha^T P A_\alpha - P]\eta_k \quad (11)$$
$$+\alpha_k^T [B_\alpha^T P B_\alpha + \sigma\beta I]\alpha_k < 0$$

Thus, the stability condition can be given by

$$\Delta V < 0 \equiv Q < 0 \quad (12)$$

We apply Schur's complement

$$Q = \begin{pmatrix} A_\alpha^T P A_\alpha - P & A_\alpha^T P B_\alpha & 0 \\ * & (\beta^{-1} I)^{-1} & 0 \\ * & * & B_\alpha^T P B_\alpha + \sigma\beta I \end{pmatrix} \quad (13)$$

With :

$$A_\alpha^T P A_\alpha - P = \begin{pmatrix} Q_{11} & Q_{12} \\ Q_{21} & Q_{22} \end{pmatrix}$$

Where:

$$Q_{11} = (A^T P_1 A + A^T P_1 B K_2 C + C^T K_2{}^T B^T P_1 A + C^T K_2{}^T B^T P_1 B$$
$$K_2 C + C^T K_2{}^T B^T P_2 B K_2 C + C^T K_2{}^T B^T P_2 L C + C^T L^T P_2 B K_2 C ++ C^T L^T P_2 L C) - P_1$$
$$Q_{12} = A^T P_1 B K_1 C + C^T K_2{}^T B^T P_1 B K_1 C + C^T K_2{}^T B^T P_2 A - C^T$$
$$K_2{}^T B^T P_2 L C + C^T K_2{}^T B^T P_2 B K_1 C + C^T L^T P_2 A - C^T L^T P_2 L C + C^T L^T P_2 B K_1 C$$

$$Q_{21} = C^T K_1{}^T B^T P_1 A + C^T K_1{}^T B^T P_1 B K_2 C + A^T P_2 B K_2 C + A^T$$
$$P_2 P L C - C^T L^T P_2 B K_2 C - C^T L^T P_2 L C + C^T K_1{}^T B^T P_2 B K_2 C +$$
$$C^T K_1{}^T B^T P_2 L C$$

$$Q_{22} = (C^T K_1{}^T B^T P_1 B K_1 C + A^T P_2 A - A^T P_2 L C + A^T P_2 B K_1 C$$
$$- C^T L^T P_2 A + C^T L^T P_2 L C - C^T L^T P_2 B K_1 C + C^T K_1{}^T B^T P_2 A$$
$$- C^T K_1{}^T B^T P_2 L C + C^T K_1{}^T B^T P_2 B K_1 C) - P_2$$

$$A_\alpha^T P B_\alpha = \begin{bmatrix} A_{11} & A_{12} & A_{13} & A_{21} & A_{22} & A_{23} \end{bmatrix}$$

With:

$$A_{11} = A^T P_1 F + C^T K_2{}^T B^T P_1 F$$
$$A_{12} = A^T P_1 B \Gamma^u + C^T K_2{}^T B^T P_1 B \Gamma^u$$
$$A_{13} = A^T P_1 B K_2 \Gamma^y + C^T K_2{}^T B^T P_1 B K_2 \Gamma^y + C^T K_2{}^T B^T P_2 B$$
$$K_2 L \Gamma^y + C^T L^T P_2 L \Gamma^y + C^T L^T P_2 B K_2 \Gamma^y$$
$$A_{21} = C^T K_1{}^T B^T P_1 F,\ A_{22} = C^T K_1{}^T B^T P_1 B \Gamma^u$$
$$A_{23} = C^T K_1{}^T B^T P_1 B K_2 \Gamma^y + A^T P_2 L \Gamma^y + A^T P_2 B K_2 \Gamma^y$$
$$- C^T L^T P_2 L \Gamma^y - C^T L^T P_2 B K_2 \Gamma^y + C^T K_1{}^T B^T P_2 L \Gamma^y + C^T K_1{}^T B^T P_2 B K_2 \Gamma^y$$

$$B_\alpha^T P B_\alpha = \begin{bmatrix} F^T P_1 F & F^T P_1 B \Gamma^u & A^T P_1 B K_2 \Gamma^y \\ * & \Gamma^{u^T} B^T P_1 B \Gamma^u & \Gamma^{u^T} B^T P_1 B K_2 \Gamma^y \\ * & * & B_{33} \end{bmatrix}$$

$$B_{33} = \Gamma^{y^T} K_2^T B^T P_1 B K_2 \Gamma^u + \Gamma^{y^T} L^T P_2 L \Gamma^y + \Gamma^{y^T} L^T P_2 B K_2$$

$$\Gamma^y + \Gamma^{y^T} K_2^T B^T P_2 L \Gamma^y + \Gamma^{y^T} K_2^T B^T P_2 B K_2 \Gamma^y$$

The following changes in variables are proposed:

$$P_2 = \mu P_1, Z = P_1 B K_2, Z_1 = P_1 B K_1, X = L^T R, Y = Z^T L,$$

$$Y_1 = Z_1^T L, W = Z^T B K_2, W_1 = Z_1^T B K_1, W_2 = Z_1^T B K_2$$

Then, inequality (9) is easily obtained.

IV. APPLICATION OF EVENT-BASED CONTROL CONDITION

For Event-based control [17] requires recomputation of the control gains and updating of the signal when (9) approaches a violation. In order to write such an equality in a convenient way, we assume that the input is held constant between successive recomputations of the FTA. In the literature this is frequently referred to as sample and hold:

$$u_k = u_{k_i} \forall k \in [k_i, k_{i+1}[, k \in N \tag{14}$$

Or the sequence $\{k_i\} i \in N$ represents the moment when the command is recalculated. Subsequently, we introduce the error «$e_1(k)$» defined by:

$$\begin{aligned} e_1(k) &= u_{k_i} - \bar{u}_k \\ e_1(k) &= u_k - \bar{u}_k + u_{k_i} - u_k \\ e_1(k) &= (0 \quad \Gamma^u \quad 0)(\alpha_{k_i} - \alpha_k) \end{aligned} \tag{15}$$

which means that

$$\alpha_{k_i} - \alpha_k = C_1^+ e_1(k) + (I - C_1^+ C) w_k \tag{16}$$

Such as: $C_1 = (0 \; \Gamma^u \; 0)$, C_1^+: is the pseudo-inverse of C_1, w_k: Arbitrary vector represents the disturbances.

From equation (5), the dynamics of the system in the interval $[k_i, k_{i+1}[$ *is given by:*

$$\begin{aligned} \dot{\eta}_k &= A_\alpha \eta_k + B_\alpha \alpha_{k_i} \\ \dot{\eta}_k &= A_\alpha \eta_k + B_\alpha \alpha_{k_i} + B_\alpha (\alpha_k - \alpha_k) \\ \dot{\eta}_k &= A_\alpha \eta_k + B_\alpha \alpha_k + B_\alpha C_1^+ e_1(k) + B_\alpha (I - C_1^+ C_1) w_k \end{aligned} \tag{17}$$

Using (12) and (17), held to :

$$J_k^T \begin{pmatrix} Q & P B_\alpha C_1^+ & P B_\alpha (I - C_1^+ C_1) \\ * & 0 & 0 \\ * & 0 & 0 \end{pmatrix} J_k \leq 0 \tag{18}$$

With $J_k^T = \begin{pmatrix} \eta_k \\ e_1(k) \\ w_k \end{pmatrix}^T$

Subsequently, the « k_i » trigger time can now be defined as the moment that this equality is satisfied:

$$J^T{}_{k_i} \Upsilon J_{k_i} = 0 \tag{19}$$

With $\Upsilon = \begin{pmatrix} Q & P B_\alpha C_1^+ & P B_\alpha (I - C_1^+ C_1) \\ * & 0 & 0 \\ * & 0 & 0 \end{pmatrix}$

Remark:

The proposed approach can be extended easily to Lipschitz nonlinear discrete-time systems. Effectively, the basic idea is to use the DMVT on the nonlinear function to transform the global nonlinear system to LPV system using *Lemma 2*. The different steps of the synthesis of feedback control laws for Lipschitz discrete-time systems are detailed are given in [18].

V. NUMERICAL SIMULATION AND RESULTS

In this section, an application on a pilot system with three tanks is given. A plant model is proposed, and the proposed control design is applied to the system. Experimental results are given to illustrate the efficiency of the developed method.

The system matrices are:

$$A = \begin{pmatrix} 1 & 0 & 0 \\ 0 & 1 & 0 \\ 0 & 0 & 1 \end{pmatrix}; B = \begin{pmatrix} 0.0649 & 0 \\ 0 & 0.0649 \\ 0 & 0 \end{pmatrix}; C = I_3$$

f simulates errors of type leak, where the matrix F is defined as:

$$F = \begin{pmatrix} 0 \\ 0 \\ 0.2626 \end{pmatrix}$$

Γ^u and Γ^y is equal to the identity matrix I. The event conditionσ rate was chosen to be equal to 5%. The initial conditions of the system and the observer are: $[0.4 \;\; 0.2 \;\; 0.3]^T$

By solving (9) using *YALMIP®*, an optimal solution is found such that the gains found are as follows:

$$L = \begin{pmatrix} 0.19005 & 0.071893 & 0.10582 \\ 0.72594 & 0.81695 & 0.51331 \\ -0.014559 & -0.069732 & 0.017343 \end{pmatrix}$$
$$\mu = 2.4052$$

5.1: No-attacks Case

First, in the figures below we show the evolution of the control u_k and various outputs $(y_1(k), y_2(k))$ without errors:

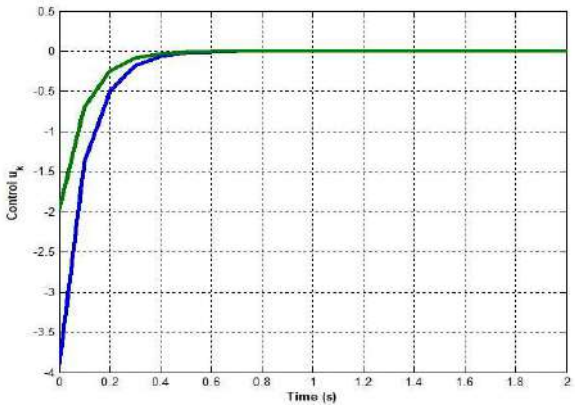

Figure 1: Evolution of the control u_k

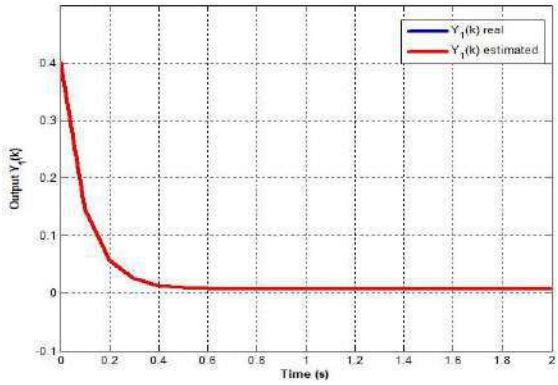

Figure 2: Evolution of the output $y_1(k)$ and its estimate

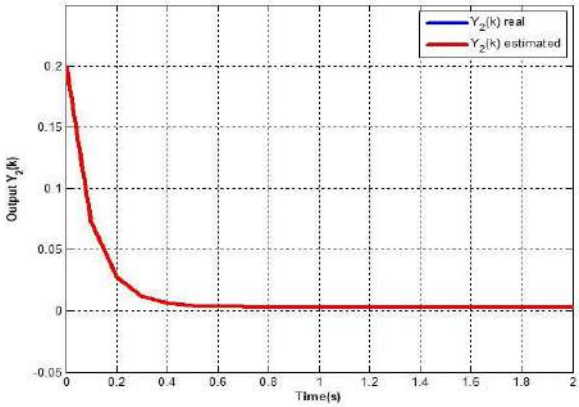

Figure 3: Evolution of the output $y_2(k)$and its estimate

From the previous figures, it is clear that the proposed output feedback control ensures the stabilization.

5.2: Case With Attacks

For this case, we apply the attack on the actuator chain and then on the sensor chain such as $b_k^u = [0.001\ 0\ ]^T$ and $b_k^y = [0.3\ 0\ 0\ ]^T$. The figures below illustrate the speed of the control u_k to reduce the impact of cyber-attacks on control and observer chains and the various outputs ($y_1(k)$, $y_2(k)$) using the trigger condition.

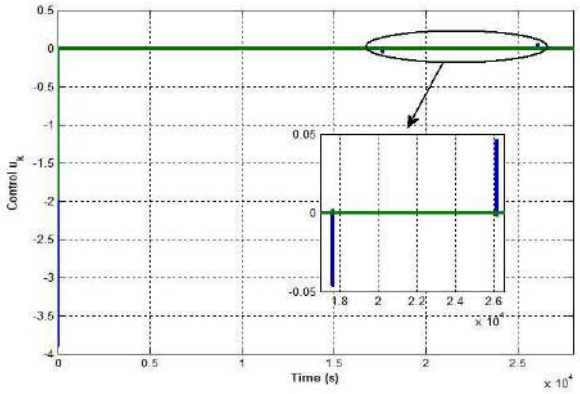

Figure 4: Evolution of the control u_k

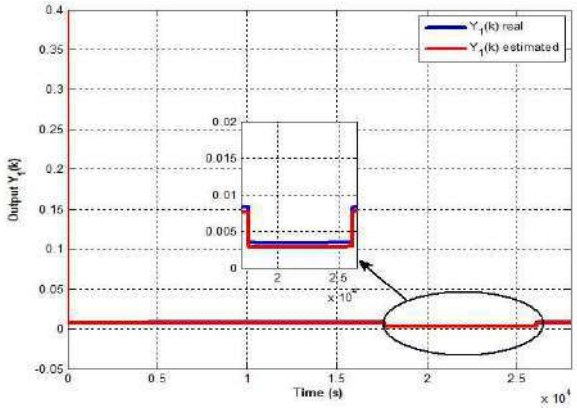

Figure 5: Evolution of the output $y_1(k)$and its estimate

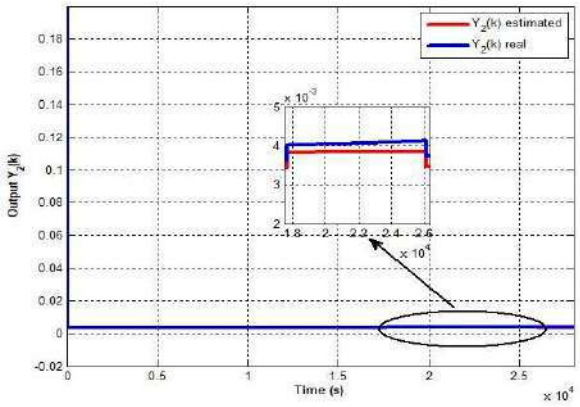

Figure 6: Evolution of the output $y_2(k)$and its estimate

The figures above illustrate the evolution of the control and the various outputs by switching the control. This ensures a reduction in the impact of attacks on the sensors and actuators, while also guaranteeing the stabilization of the interconnected system around its equilibrium point. So, it is clear that the first step in detecting and identification of attacks has been reached.

VI. CONCLUSION

Based on an event triggered control system, this paper presents an attack/fault tolerant control system. By studying the stability using the BMIs framework and designing the observer, the feedback controller that calculates the control inputs is obtained. The triggering mechanism for the control input must be deduced when the error exceeds a chosen threshold. Thus, a numerical validation on a three-tank system that is subject to disturbances and to an attempt of data falsification on the sensor and the actuator is considered with satisfactory results. In addition, a residual generator and an observer have been used to detect faults and to isolate attacks. The extension of the proposed synthesis methods with nonlinear output and the generalization of the proposed method for robust schemes could be a direction for further studies.

REFERENCES

1. A. Thabet, G.B.H. Frej, K. Mansouri, E. Chauveau, S.B.H. Abdallah, Estimation des défauts pour les systèmes non linéaires interconnectés: Application à un réseau électrique, SGE21, Symposium de Génie Electrique, Nantes, France. Jul 2021; (hal-03013579).
2. Gupta, P., Singh, N., Mahajan, V. Intrusion Detection in Cyber-Physical Layer of Smart Grid Using Intelligent Loop Based Artificial Neural Network Technique, International Journal of Engineering. 2021;34(5), pp.1250-1256. doi:10.5829/ije.2021.34.05b.18.
3. S. Bezzaoucha Rebaï, H. Voos and M. Darouach. A contribution to Cyber-Security of Networked Control Systems: an Event-based Control Approach. In Proc. The 3rd International Conference on Event-Based Control, Communication and Signal Processing, Madeira, Portugal. 2017; DOI: 10.1109/EBCCSP.2017.8022805.
4. DAS, D., & Savier, J. A Multi-Objective Method for Network Reconfiguration (TECHNICAL NOTE). International Journal of Engineering. (2009); 22(4), 333-350.
5. K. Liu ,H. Guo, Q. Zhang, and Y. Xia, A Survey of Cyber Attacks on Cyber Physical Systems: Recent Advances and Challenges, IEEE/CAA J. of Automatica Sinica. 2022; Vol. 9, No. 5, pp. 784–800.
6. Y. Mo, S. Weerakkody, and B. Sinopoli. Physical authentication of control systems designing watermarked control inputs to detect counterfeit sensor outputs. IEEE Control Systems. 2015; pages 93 –109.

7. K. Zhang and E.Braverman. Delayed impulsive stabilisation of discrete-time systems: a periodic event-triggering algorithm." International Journal of Control. 2023; p. 1-11.
8. Keshavarz, M., Doroudi, A., Kazemi, M., & Mahdian Dehkordi, N. A New Consensus-based Distributed Adaptive Control for Islanded Microgrids. International Journal of Engineering. (2021); 34(7), 1725-1735. doi: 10.5829/ije.2021.34.07a.17.
9. A. Teixeira, I. Shames, H. Sandberg, and K.H. Johansson. A secure control framework for resource-limited adversaries. Automatica. 2015; 51:135–148.
10. F. Pasqualetti, F. Dörfer, and F. Bullo. Cyber-physical security via geometric control: Distributed monitoring and malicious attacks. In IEEE Conference on Decision and Control, Hawai, USA, 2012.
11. A. Rosich, H. Voos, and Darouach, M. Cyber-attack detection based on controlled invariant sets. In European Control Conference, Strasbourg, France, 2014.
12. R.S. Smith. Covert misappropriation of networked control systems. IEEE Control Systems. 2015; 35(1):82–92.
13. Asgari, S., Menhaj, M., Suratgar, A. A., & Kazemi, M. A Disturbance Observer Based Fuzzy Feedforward Proportional Integral Load Frequency Control of Microgrids. International Journal of Engineering.2021; 34(7), 1694-1702. doi: 10.5829/ije.2021.34.07a.13.
14. E. Hassine, A. Thabet, N. GASMI, G.B.H. Frej et B. Metoui. Cyber-attack Tolerant Control of Complex Interconnected Systems: Output Feedback Stabilization Approach.In: 2023 IEEE Int. Workshop on Mechatronic Systems Supervision (IEEE IW_MSS'23), 02-05 November 2023, Hammamet- Tunisia, p. 1-5.
15. Khettache, L., & Abdessemed, R. A New Speed Control Approach of Linear Induction Motor Based on Robust RST Controller and Model Reference Adaptive System Estimator. International Journal of Engineering. 2023; 36(4), 630-639. doi: 10.5829/ije.2023.36.04a.03.
16. A. Thabet, G.B.H. Frej, E.Hassine. "Stabilisation des Systèmes Non Linéaires de Lipschitz dans la Représentation d'Etat Réciproque" In Ingénierie des Systèmes: Modélisation, Commande et Supervision (ISMCS'22), Djerba-Tunisie, 2022.
17. Zhang, K., Braverman, E. and Gharesifard, B."Event-triggered control for discrete-time delay systems." Automatica, 2023; vol. 147, p. 110688.
18. Thabet, A., Hassine, E., Gasmi, N., Frej, G.B.H., Boutayeb, M. LMI-Based Designs for Feedback Stabilization of Linear/Nonlinear Discrete-Time Systems in Reciprocal State Space: Synthesis and Experimental Validation. In: State Estimation and Stabilization of Nonlinear Systems: Theory and Applications. Cham: Springer Nature Switzerland. 2023; p. 205-219. https://doi. org/10.1007/978-3-031-37970-3_11.

Physic-Mechanical Properties of Petroleum Road Bitumen Modified with Styrene-Butadiene Rubber, Butyl Rubber and Nano-Sized Dolomite

Dr. Shixaliyev Kerem Seyfi

Azerbaijan State Oil and Industry University

ABSTRACT

In this work, road petroleum bitumen was modified with styrene butadiene rubber, butyl rubber and nano-sized dolomite. As a result of the modification, the basic physical, mechanical and chemical characteristics of the resulting composition were improved. It has been shown that the penetration, softening temperature and adhesive properties of bitumen as a result of modification with polymers are improved by 1.3 times compared to standard unmodified bitumen. The use of rubbers such as butyl rubber, styrene butadiene rubber and dolomite improves the mechanical strength and adhesive properties of road bitumen. Thus, the resulting polymer bitumen is an excellent binding system for the resulting asphalt-bitumen mixture.

Keywords: bitumen, modification. styrene- butadiene rubber, butyl rubber, rubber waste, polymer-bitumen composition, physical and mechanical properties, dolomite.

Classification: DCC Code: 624.1

Language: English

Great Britain Journals Press

LJP Copyright ID: 392953
Print ISSN: 2631-8474
Online ISSN: 2631-8482

London Journal of Engineering Research

Volume 24 | Issue 4 | Compilation 1.0

Physic-Mechanical Properties of Petroleum Road Bitumen Modified with Styrene-Butadiene Rubber, Butyl Rubber and Nano-Sized Dolomite

Dr. Shixaliyev Kerem Seyfi

ABSTRACT

In this work, road petroleum bitumen was modified with styrene butadiene rubber, butyl rubber and nano-sized dolomite. As a result of the modification, the basic physical, mechanical and chemical characteristics of the resulting composition were improved. It has been shown that the penetration, softening temperature and adhesive properties of bitumen as a result of modification with polymers are improved by 1.3 times compared to standard unmodified bitumen. The use of rubbers such as butyl rubber, styrene butadiene rubber and dolomite improves the mechanical strength and adhesive properties of road bitumen. Thus, the resulting polymer bitumen is an excellent binding system for the resulting asphalt-bitumen mixture.

Keywords: bitumen, modification. styrene-butadiene rubber, butyl rubber, rubber waste, polymer-bitumen composition, physical and mechanical properties, dolomite.

Author: Doctor of Technical Sciences, Professor-Academician of the European Academy of Natural Sciences. Professor, Department of Organic substances and technology of macromolecular compounds. Azerbaijan State Oil and Industry University Baku, AZ1010, Azerbaijan, 20 Azadlig Avenue.

I. INTRODUCTION

Petroleum road bitumen change their physical and chemical parameters in a wide range (temperature, frost resistance, ductility, elasticity, adhesive bond, resistance to aggressive environments, high dielectric strength, etc.) and, compared to their low cost, allow them to be used in various areas.

Petroleum bitumen can be used in agriculture, construction and many other industries [1-4].

The bitumen used when gluing waterproofing is a residue from the distillation of petroleum products. It is a hard-looking, black, shiny mass that, under prolonged loads, retains its ductility even at low temperatures [5-7].

Over time, during storage and under operating conditions under the influence of sunlight and oxygen, the composition and properties of bitumen change: the relative content of solid and brittle components in them increases and, accordingly, the amount of oily and resinous fractions decreases, therefore the amount of oily and resinous fractions decreases. resinous fractions. increased fragility and hardness (aging process). Therefore, the process of bitumen modification is very relevant [8-10].

The properties of bitumen can be improved by combining them with polymer additives [11]. Currently, in the construction of roads for the production of asphalt concrete pavements, bitumen-polymer compositions are used as a binder, and for this purpose the expensive polymer thermoplastic elastomer DST-30 is used [12-13]it is necessary to find more economically beneficial modifiers for road bitumen [14-16].

Typically, road petroleum bitumen has a plasticity range, as a rule, no higher than 60-65 C, which is clearly not enough for the construction of outer layers of coating in the climatic conditions of most regions. In addition, viscous road bitumen practically does not have elastic properties that determine the resistance of composite materials, such as asphalt concrete, to destruction under cyclic loading. Therefore, bitumen binders

fundamentally require modification and improvement of physical and mechanical properties, since by their nature they cannot provide the necessary durability of asphalt concrete road surfaces under conditions of increasing traffic loads [17-19].

Based on a set of indicators, polymers and their waste have the greatest potential for improving the properties of bitumen binders.

II. METED AND DISSERTATION

To modify oil bitumen grades ROB 25/40, TB 70/30 and Baku 85/25, rubber, rubber waste and nano-sized dolomite were used. The recipe and composition of the components are given in Tables 1, 2 and 3, and the physical and mechanical properties of the bitumen used are given in Table 4.

Subsequently, based on the obtained compositions, an asphalt concrete mixture was prepared using mixing equipment

Table 1: The composition of the composition based on rubber crumb (RC)

Name of Components	№ Samples					
	1			4	5	
	The content of the mass parts					
Bitumen	100	100	100	100	100	
BR+BSR+rubber waste (2%+3%+8%)	2			8	10	
Sulfur+	1,5					
nano-sized dolomite	-	1,5 2,0	1,5 2,0	1,5 2,0	1,5 2,0	

Dolomites are a sedimentary rock that includes dolomite itself - CaCO3·MgCO3, with admixtures of clayey, ferruginous, siliceous and other substances. Dolomites come in granular, politic and crystalline structures. The hardness of dolomite is slightly higher than the hardness of limestone, its density is 2.0 - 2.8 g/cm3, and its tensile strength ranges from 120 - 300 MPa. Dolomite has a white, greenish-brown, brown and reddish-brown color. Taking into account the above, it must be assumed that it can be more effective than limestone materials when constructing structural layers of road and airfield pavements.

Different quantitative ratios of calcium carbonates in sedimentary rocks are one of the reasons for the wide variety of mineral-petrographic and physical-mechanical characteristics of these rocks, the name of which depends on the percentage of calcium carbonate in them, which is clearly shown in Table. 2.

Table 2: Content (% by weight) of calcium carbonate in limestone and dolomite

Name of Mineral	Standard for carbonate, in % by weight					
	Pure Limestone	Dolomite Limestone	Dolomite Limestone	Calcareous Dolomite	Calcareous Dolomite	Pure Dolomite
$CaCO_3$	90-100	75-95	50-75	25-50	5-25	0-5
$CaCO_3$ $MgCO_3$	0-10	5-25	25-50	50-75	75-95	95-100

The mechanical properties of limestones play a significantly important role in road and airfield construction, since these properties depend on the strength and cementing ability of the carbonate rocks they contain, as well as on the presence of non-carbonate impurities, which, in each individual case, are characterized by the chemical composition of the specific limestone material .

The composition of the composition based on the components we use is given in Table 3.

Table 3: Composition of bitumen-polymer compositions

Composition Components	The Content of Components, Mass. H. By Examples								
	1	2	3	4	5	6	7	8	9
Rubber crumb+Br+BSR	-	5	10	15	20	25	30	35	40
Bitumen	200	200	200	200	200	200	200	200	200
Filler	200	200	200	200	200	200	200	200	200
nanoclay+wooden stone(1+1)	150	-	-	-	10	10	10	10	10
The mixing temperature of the components in the mixer, ° C	100	70	90	100	160-180	70	90	70	100
Mixing time, min	15	10	12	15	65-120	10	12	10	15

As laboratory studies have shown, the introduction of 2 wt.% active rubber powder into grade A asphalt with good properties leads to a doubling of its softening temperature, while the frost resistance and elasticity of asphalt concrete increase.

Rubber, being an elastomeric material with a unique set of properties, only improves the durability of polymer-asphalt concrete.

In our work, the main attention was paid to improving the properties of domestic low-quality oxidized bitumen. The introduction of polymers and their waste leads to a sharp increase in the properties of Indicators of physical and mechanical properties of asphalt mixtures.

As laboratory studies have shown, the introduction of 2 wt.% active rubber powder into grade A asphalt with good properties leads to a doubling of its softening temperature, while the frost resistance and elasticity of asphalt concrete increase.

Rubber, being an elastomeric material with a unique set of properties, only improves the durability of polymer-asphalt concrete.

In our work, the main attention was paid to improving the properties of domestic low-quality oxidized bitumen.

The introduction of polymers and their waste leads to a sharp increase in the properties of bitumen (Tables 4 and 5).

Table 4: Physic-mechanical properties of a composition based on polymers and bitumen

№	Indicators	Samples				
		1	2	3	4	5
1.	Penetration of a needle at 25 ° C	38	72	100	71	96
2.	Softening point, ° C	49	68	82	56	75
3.	Fragility temperature, ° C	-10	-10	-26	-8	-20
4.	Tensile at 25 ° C	40	60	70	55	60
5.	Density, g / cm 3	2,34	2,36	2,38	2,2	2,4
6.	Temperature changes at T = 65 ° C for 5 hours	7	6	6	6	6
7.	Tensile strength at 20 ° C at 50 ° C	2,4 0,9	3,0 1,0	3,5 1,2	3,1 1,1	3,4 1,3

Table 5: Indicators of physical and mechanical properties of asphalt mixtures

Indicators	Indicator Values for Examples								
	1	2	3	4	5 prototype	6	7	8	9
Tensile strength, MPa	4,5	10,0	6,0	6,5	Breaks without load	7,0	8,0	5,0	9,5
Elongation at break,%	650	850	1100	780	-	900	900	700	830
Shore A hardness, Con, unit, усл. Ед	63	50	35	58	20	45	43	40	45
Polymer fluidity T=190 °C, P=49 H, q/10 min	18	20	40	35	100	30	35	30	25

The introduction of crumb rubber in bitumen allows to obtain a binder, which provides a significant improvement in the deformability and crack resistance of asphalt concrete.

Table 6: Physical -mechanical properties of crushed stone-mastic asphalt concrete with the introduction of Thermoplastic Polyethylene on stone materials

№	The name of indicators	Norms on Standard	0 %	0,1 %	0,2 %	0,3 %	0,5 %
			Thermoplastic Polyethylene				
1	Density (bulk density), g / cm3	-	2,39	2,40	2,40	2,41	2,41
2	Residual porosity, %	2,0–4,0	3,761	3,358	3,358	2,956	2,956
3	Water saturation, % by volume	1,5–4,0	2,82	2,33	2,23	2,16	2,01
4.	Tensile strength in compression, MPa at temperature: 200 ° C 500 ° C	- 2,5-0,70	3,29 0,75	3,52 0,87	3,67 1,00	3,99 1,11	4,12 1,12
5.	Water resistance coefficient	-	0,86	0,92	0,94	0,95	0,97

6.	The coefficient of water resistance during prolonged water saturation (15 days.)	0,75	0,79	0,86	0,88	0,91	0,92
7.	Fracture resistance - tensile strength at split at a temperature of 0 ° C, MPa	3,0 – 6,5	3,48	3,82	3,99	4,21	4,16
8.	Coefficient of internal friction tg	0,94	0,89	0,90	0,92	0,92	0,91
9.	Shear grip at 500 ° C, MPa	0,20	0,18	0,33	0,57	0,60	0,65
10.	The binder runoff index,%	0,20	0,24	0,19	0,18	0,15	0,13

The values of structural and rheological constants were established as a result of testing coating samples and constructing rheological curves (Table 7).

Table 7: Structural and rheological constants

	Coating 1 (bitumen)				Coating 2 (polymerbi Bumen)			
t^0, C	E_y, Po	E_3, Po	θ, c	α_k, 1/degrees	E_y, Po	E_3, Po	θ, c	α_k, 1/degrees
+20°C	$2,5\text{-}10^6$	$2,18\text{-}10^6$	$4,6\text{-}10^2$	$4,3\text{-}10^2$	$5,76\text{-}10^6$	$5,02\text{-}10^6$	$1,4\text{-}10^2$	$2,95\text{-}10^4$
+10°C	$6,3\text{-}10^6$	$5,45\text{-}10^6$	$11,1\text{-}10^2$	-	$7,9\text{-}10^6$	$6,84\text{-}10^6$	$3,39\text{-}10^2$	-
0°C	$1,55\text{-}10^7$	$1,15\text{-}10^7$	$27,2\text{-}10^2$	-	$1,41\text{-}10^7$	$1,05\text{-}10^7$	$8,3\text{-}10^2$	-
-10°C	$3,9\text{-}10^7$	$2,94\text{-}10^7$	$1,51\text{-}10^3$	-	$2,59\text{-}10^7$	$1,95\text{-}10^7$	$1,55\text{-}10^3$	-
-20°C	$9,9\text{-}10^7$	$2,07\text{-}10^7$	$5,7\text{-}10^4$	-	$3,08\text{-}10^8$	$6,45\text{-}10^7$	$1,74\text{-}10^3$	-
Thunderstorm during rain	$6,3\text{-}10^6$	$6,3\text{-}10^6$	$11,1\text{-}10^2$	-	$7,9\text{-}10^6$	$6,84\text{-}10^6$	$3,39\text{-}10^2$	-

Calculations of temperature stresses arising in coatings at different temperatures are given in table 8

Table 8: Temperature stresses in coatings

Stress σ_t	σ_t in the temperature range, Pa					
Type Covered	+20°C	+10°C	0°C	-10°C	-20°C	Thunderstorm
Oil Polymer bitumen 70/30)	4,86	12,24	27,7	70,24	90,7	62,5
Polymer bitumen "The cream"	5,57	7,62	12,5	2,14	43,36	38,17

: n the work, the further study was to determine the durability of the resulting polymer-phaltobitumen system. The calculation is based on assumptions under which temperature and stress change continuously, and the destruction process is irreversible according to the Bailey criterion (the principle of summation of stresses). Under the influence of various stresses, the material loses a certain amount of strength each time, and when the amount reaches unity, it collapses.

After determining the durability values of coatings at different temperatures depending on the operating stresses, the overall durability of the materials was determined using the formula

$$\tau_{(\sigma,t)} = \frac{100}{\frac{P_1}{\tau_1} + \frac{P_2}{\tau_2} + \ldots + \frac{P_n}{\tau_n} + \frac{g}{\tau_g}}$$

where $P_1, P_2 \ldots P_n$ is the percentage of days in a year with a temperature of $T_1, T_2 \ldots T_n$; $\tau_1, \tau_2 \ldots \tau_n$ -durability of the material, respectively, at temperatures $T_1, T_2 \ldots T_n$.

III. RESULT

Thus, the computational and experimental method for predicting the durability of a coating comes down to an experimental study of the properties of the coating material under various test conditions and further calculation of the durability of these coatings.

This paper presents the results of computational and experimental studies of the durability of coatings made of various materials:

Since the most common cause of destruction of asphalt concrete is the formation of cracks due to the difference in temperature deformations of the coating and the base or the coating layer and the base, Comparison of standard properties of asphalts with polymer-bitumen coating mass was reduced to determining changes in structural-rheological and physical-mechanical properties, including weather resistance and water resistance, and, as a consequence, service life and reliability. of these materials has been determined.

It has been shown that to improve the performance of highways and their durability it is necessary to modify them with polymers such as BR and BSR.

REFERENTS

1. Belyaev P.S., Zabavnikov M.V., Malikov O.G., Volkov D.S. / Bulletin of the Tambov State Technical University. -2005.-T. 11. - No. 4. -FROM. 923-930.11.
2. Timofeev A.G. The effect of complex modification by processing products of secondary rubber materials and polymer waste (PET) on the properties of road bitumen // Vestnik TSTU. - Tver, -2017, - issue 4.-C.7-11.
3. Zolotarev V.A. About quality indicators of bitumen modified with polymers - Kiiv, -2006 r - (Zbirnik of scientific articles); - sleep. 5; -C.200-231.
4. Amirov Fariz Ali., Shixaliyev Kerem Sefi., Obtaining and application of rubber mixtures based on isoprene and functional group polymers. Austrian Journal of Technical and Natural Sciences Vienna. 2017.-№3-4.- P.274 technology journal Kemerovo. -2017., - 46 p.
5. Shikhaliev K.S. Modification of petroleum bitumen with polymer waste. Exact science and 15. Shykhaliev K. S. Alieva Z. N., Modification of petroleum bitumen with plastic waste. Problem of modern science and education 2017. 58p.
6. Kerem Shixaliyev Investigation of the subsequent use of lands along the Araz River contaminated with heavy metals, JOURNAL OF AERONAUTICAL MATERIALS ISSN: 1005-5053, Vol. 43, Issue-01, 2023pp. 102-111
7. Kerem Shixaliyev, RESEARCH AND APPLICATION OF THE PROCESS OF MODIFYING OIL ROAD BITUMEN WITH POLYMERS FOR USE AS A BINDER, ION EXCHANGE AND ADSORPTION ISSN: 1001-5493, Vol. 23, Issue-01, 2023 pp.248-255.

8. Kerem Shixaliyev Research New Ways of Processing Polymer Waste that was Formed as a result of Operation, *Novel Perspectives of Geography, Environment and Earth Sciences Vol. 1*2022, Page 25-35.
9. *Kerem Shixaliyev. PROPERTIES OF THE COMPOSITION BASED ON MODIFIED POLYETHYLENES,* Eur. Chem. Bull. *ISSN 2063-5346, 2023; Volume -12, Special Issue-5 : Page: 242-258.*
10. *Kerem Shixaliyev*. Study of the Properties of the Composition Obtained Based on Mixtures of Polyvinyl Chloride and Ethylene-Propylene Copolymers, International Journal of Current Science Research and Review ISSN: 2581-8341 *Vol 6 No 1 (2023): Volume 06 Issue 01 January 2023,pp314-318.*
11. *Kerem Shixaliyev*. Studies of the physical and mechanical properties of the composition obtained based on polyvinyl chloride, synthetic rubber ethylene propylene terpolymer, and plasticizer, Qeios Ltd. All rights reserved. Qeios, CC-BY 4.0 Article, March 21, 2023pp.1-9
12. *Kerem Shixaliyev*. DİSCONTİNUED HİGH-DENSİTY AND LOW-DENSITY POLYETHYLENE PURCHASE OF ENVİRONMENTALLY FRİENDLY ROAD SURFACES, European Chemical Bulletin ISSN 2063-5346, Section A-Research pape2023,12(Special Issue 1), 654-662.
13. *Kerem Shixaliyev*. Environmental Damage Of Polymer Products That Have Been Turned Into Assembly After Being Out Of Use, European Journal of Molecular & Clinical Medicine ISSN 2515-8260, Volume 09, Issue 08, 2022 pp. 1965–1980.
14. *Kerem Shixaliyev*. ENVIRONMENTAL DAMAGE OF POLYMER PRODUCTS THAT HAVE BEEN TURNED INTO ASSEMBLY AFTER BEING OUT OF USE, *Environmental Issues: Innovations in Life Sciences in Today's World,* 3First Impression: January 2023 pp32 – 39.
15. *Kerem Shixaliyev*. Investigation of the Properties of a Composition Obtained based on Mixtures of Polyvinylchloride and Synthetic Rubber Ethylene Propylene Terpoliymer, Medicine editor *special issue eurchembull,* Vol. 11: Number 1, 2023 JCLMM 1/11 (2023) |2653–2658.
16. *Kerem Shixaliyev*. DİSCONTİNUED HİGH-DENSİTY AND LOW-DENSITY POLYETHYLENE PURCHASE OF ENVİRONMENTALLY FRİENDLY ROAD SURFACES, European Chemical Bulletin ISSN 2063-5346, Section A-Research pape 2023, 12(Special Issue 1), 654-662.
17. *Kerem Shixaliyev*. eneralization of the temperature dependence of some physical properties of high-strength polyethylene using the method of given parameters/ Journal of Harbin Engineering University ISSN: 1006-7043. *Link1:* https://harbinengineering journal.com/index.php/journal/article/view/ 2429, Vol 45 No. 1 January 2024 *Page* 431 – 438.
18. *Kerem Shixaliyev*. Discontinued High-density and Low-density polyethylene purchase of environmentally friendly road surfaces, Journal of Harbin Engineering University ISSN: 1006-7043 Vol 45 No. 1 January 2024 *Page № 1:* 422 – 430.
19. *Kerem Shixaliyev*. DETERMINATION OF RUBBER-CORD CONNECTION ON THE BASIS OF LATEX SYNTHESIZED ON THE BASIS OF ETHYLENE-PROPYLENE RUBBER, China Petroleum Processing and Petrochemical Technology, Catalyst Research Volume 24, Issue 1, March 2024 Pp. 117-126ISSN**:** 1008-6234. https://zgsyjgysyh-gjs.cn/index.php/reric/article/view/2024-117.html

This page is intentionally left blank

Scan to know paper details and author's profile

Improvement of Wear Resistance Properties of Metal Gears using Laser Surface Hardening

Abbos Elmanov, Davron Tojiyev, Sirojiddin Kengboyev, Nazirjon Safarov & Adham Norkobilov

ABSTRACT

This study investigates the efficacy of laser surface hardening (LSH) as a method to enhance the wear resistance of metal gears, comparing it with traditional hardening techniques such as induction and flame hardening. The LSH process involves using a high-energy laser beam to rapidly heat the gear surface, resulting in microstructural changes that increase hardness and wear resistance. Experiments were conducted using two common gear steels, JIS-SCM415 and JIS-S45C, with the laser parameters optimized to achieve the desired hardness profile. The results showed that the best hardening was achieved with a laser power of 1000W, scanning speed of 100mm/s, and a spot size of 1mm, resulting in a surface hardness of 672 HV and a core hardness of 502 HV. Wear testing indicated that the wear rate of laser-hardened gears was comparable to new conventional gears, with a weight loss of 10-12 mg/hr. The study demonstrates that LSH can significantly improve the wear resistance of gears, with minimal distortion and precise control over the hardened depth, making it a promising alternative to conventional hardening methods for enhancing gear longevity and performance.

Keywords: laser surface hardening; wear resistance; metal gears; surface hardness; microstructural changes; gear steels; hardening parameters; wear testing; gear material properties; surface treatment techniques.

Classification: DCC Code: 621.8

Language: English

Great Britain Journals Press

LJP Copyright ID: 392954
Print ISSN: 2631-8474
Online ISSN: 2631-8482

London Journal of Engineering Research

Volume 24 | Issue 4 | Compilation 1.0

Improvement of Wear Resistance Properties of Metal Gears using Laser Surface Hardening

Abbos Elmanov, Davron Tojiyev[α], Sirojiddin Kengboyev[σ], Nazirjon Safarov[ρ] & Adham Norkobilov[ω]

ABSTRACT

This study investigates the efficacy of laser surface hardening (LSH) as a method to enhance the wear resistance of metal gears, comparing it with traditional hardening techniques such as induction and flame hardening. The LSH process involves using a high-energy laser beam to rapidly heat the gear surface, resulting in microstructural changes that increase hardness and wear resistance. Experiments were conducted using two common gear steels, JIS-SCM415 and JIS-S45C, with the laser parameters optimized to achieve the desired hardness profile. The results showed that the best hardening was achieved with a laser power of 1000W, scanning speed of 100mm/s, and a spot size of 1mm, resulting in a surface hardness of 672 HV and a core hardness of 502 HV. Wear testing indicated that the wear rate of laser-hardened gears was comparable to new conventional gears, with a weight loss of 10-12 mg/hr. The study demonstrates that LSH can significantly improve the wear resistance of gears, with minimal distortion and precise control over the hardened depth, making it a promising alternative to conventional hardening methods for enhancing gear longevity and performance.

Keywords: laser surface hardening; wear resistance; metal gears; surface hardness; microstructural changes; gear steels; hardening parameters; wear testing; gear material properties; surface treatment techniques.

Author α σ ω: Shahrisabz branch of the Tashkent chemical-technological institute.
ρ: Namangan Institute of Engineering and Technology.

I. INTRODUCTION

There are four directions of hardness enhancement techniques, namely: solid-state phase transformation hardening, surface coating, chemical heat treatment, and surface hardening [1], [2]. Laser surface hardening (LSH) is a newly developed surface hardening process that provides an effective means to increase the wear resistance of gear material [3]. This is a process in which a focused coherent high-energy beam is used to rapidly heat the metal at the surface to a temperature which is above the transformation temperature and the melting point, but which is well below the temperature of the entire workpiece. The laser heat source is moved over the surface in a regular pattern and then the part is either water or air cooled. The change in the microstructure of the substrate induced by the cooling rate of the treated area, which is controlled by the thermal diffusivity of the material and the laser scanning speed [4].

Typically, the laser hardening process involves the heating and cooling time of the order of microseconds up to milliseconds [5]. By selecting suitable processing parameters, various microstructures and hardness profiles can be obtained. If the gear made of through-hardening steel like JIS-SCM415 is subjected to the through-hardening heat treatment, which offers the highest possible wear resistance, the hardness profile obtained by the laser hardening process should be similar to the through-hardening profile. Although the basic principle of the laser hardening process is well understood, the prediction of the optimum process parameters and the evaluation of the gear's micro-macro hardness profile have not been established due to

a lack of knowledge on the kinetics of the heating and cooling of the gear material and the measurement method of the thermal physical properties of the work material [6]. The microstructure changes caused by the laser surface hardening process are complex and diverse. Compared with the usual hardening process such as quench hardening, with that in mind, it is understood that the hardness of the laser-treated area and the wear resistance do not correlate simply, and most of the previous studies report that the wear test produces better results than the hardness test [7]. Since it is incredibly difficult to directly evaluate the gear tooth surface, we will examine the wear resistance of the pin-on-disk wear test and clarify the correlation between the wear micro-macro area and the hardness profile to provide a measurable method in the evaluation of the gear's micro-macro hardness profile, thus obtaining the optimum process parameters and the hardening design that creates the minimum gear wear in any situation.

1.1 Background

Laser hardening, compared to other surface heat treatments such as induction and flame hardening, offers several advantages. Laser hardening is applicable for irregular surfaces and complicated shapes, as the heat source from the laser can be controlled easily. It can also be used for local hardening or hardening only in specific areas [8]. This is important because only the surface of the gear needs to be hardened. In previous research, the steel manufacture of material gears has been used from cheap steels to expensive alloy steel. This is interesting for study because the method of hardening can affect the properties of the material, and possibly the method can be used in hardening other materials such as iron and steel cast, or even stainless steels.

Gears needing wear and pitting resistance means we require higher surface hardness. As the gears' loading condition assumes that the hardness value of the core and surface are considered the same, this will make the contact stress of the gear very high, which affects the hardness of the material around the area. Under these conditions, high contact stress promotes the gear's surface to be worn and decreases the hardness. High hardness of the gear surface means we also need to consider the ability to deliver good fatigue resistance and abrasive wear resistance. This is different from the characteristic of through hardening as it is better used for case hardening with the gear.

In recent years, the investments in the machinery industry have escalated the manufacture of mining, construction, oil and gas machinery equipment, and methods to process metal surfaces that can change the properties and increase their performance lifespan. In these industries, metal gears have been long used as they are suitable for harsh conditions and heavy loading. Gears are usually made from low carbon steels with sufficient strength and toughness.

1.2 Objective

The procedure to be followed in this work for obtaining the above expected result is as follows:

1. Selection of processing parameters of the laser such as beam diameter, power, speed, and spot size. With these parameters, a small portion of the surface of the gear is heated and then it can be quenched immediately by contact from the rest of the material, resulting in microstructure changes.
2. Gear samples will be checked for various microstructures and hardness between small variations of laser parameters;
3. The wear resistance of these selected simulated microstructures will be tested in the laboratory and conducted field tests;
4. The wear rate of these gears will be used to compare it to the previous gears by preparing a dual block between two gears and loading it by means of a spring and applying rotational motion. This whole procedure is done to test the toughness of microstructures of gears.

II. LITERATURE REVIEW

Gears are mechanical components used to transmit motion between rotating shafts. Most often, gears are used to increase or decrease the torque, increase or decrease the speed, and/or change the direction of the shaft rotation [9]. There are many different types of gears such as

spur gears, worm gears, bevel gears, etc., that are used in a variety of appliances. Gears are generally made out of metal due to the high strength characteristics [10]. Steel is most often used due to its high strength and low cost. Gears are subject to a unique form of wear called macropitting, for which few treatment options exist, and tooth breakage, which can generally be prevented through increasing the hardness of the gear [11].

Gears enable the transmission of motion and power between rotating shafts. However, they are often regarded as weak components in machinery and are susceptible to failure through a variety of failure modes [12]. Each gear has its own specific gear tooth design. While each design has different applications and performance requirements, they all will encounter wear. Just a few examples of the types of gears are bevel, helical, spur, and worm gears [13]. Wear can vary from being a marginal concern for some applications to being a crippling problem for others. Even though wear is an undesirable phenomenon, it can be used as an end-of-life indicator for some applications when catastrophic failure is a possibility [14].

Wear is defined as a surface degradation involving the progressive loss of material from a solid body while it remains in repetitive contact with another body. There are a variety of wear forms that affect gears such as abrasive wear, adhesive wear, and pitting. These wear forms are caused by contact stress [15]. High contact stress often causes surface fatigue and gear failure as the objects slip to a rolling motion. It is estimated that 85% of gear failures are the result of surface fatigue.

Gears can fail from pitting fatigue, with an incidence rate as high as 28%. Pitting damage is related to the loss of surface strength and is characterized by the formation of surface cavities and eventual removal of surface material from adhesive wear [16]. Gears subject to pitting exhibit increased surface roughness and noise and generally cannot meet the intended gear life.

Pitting can cause complete tooth failure or failure of the entire gearbox. The various types of metal gears have different wear resistance properties and for certain applications, it may be necessary to enhance these properties in order to increase the useful life of the gear [17].

When comparing modern hardening techniques, laser beam hardening is relatively new, emerging in the 1980s [18]. However, its use is increasing in industry, particularly in the automotive and machine tool industries. It is a selective hardening process using a laser as a heat source. The process is normally conducted using a CNC machine, allowing a precise hardened area to be achieved. Gears are an ideal candidate for laser hardening because their geometry allows heat to be applied to precise locations, with minimal thermal effect on the surrounding area, enabling production cost reduction [19]. The aim of laser hardening is to increase the wear resistance of the gear surface and improve fatigue strength. This is achieved by the rapid heating and subsequent rapid cooling of the surface that changes the microstructure only in the surface layer, resulting in increased hardness and wear resistance. By careful selection of process parameters, a range of microstructures can be achieved to suit the particular gear application. A key advantage of laser hardening over conventional hardening methods is the minimal distortion that occurs due to the localized heating and cooling [20]. This is a significant benefit, allowing closer dimensional tolerances to be held, reducing or even eliminating the need for post-hardening finishing operations. The hardening depths can be more closely controlled than by conventional methods, typically ranging from 0.8-1.2 times the laser spot diameter [21].

However, this can be adjusted by multiple scans of the laser to achieve greater depths if required. This contrasts with conventional case hardening that often results in a thin, hard surface layer but with a significant predetermined risk of distortion to the part and a shallow hardened depth.

III. MATERIAL AND METHODS

Laser surface hardening is a recent addition to the induction hardening process, which uses a focused infrared laser to heat the surface of steel, with the heating rate and cooling rate are extremely high. When the laser stops heating the surface, the steel will cool extremely fast to room

temperature. This will produce a martensitic structure at the surface. Depending on the heating rate and energy input, it is possible to harden to a depth between 0.5 to 3mm. This method is very favorable for only hardening the surface because it does not require any masking or post-cleaning process. The high cooling rate also minimizes part distortion. In this research, Rofin DC-015 diffusion cooled CO_2 slab laser and a max pulse energy of 1.8kJ were used. In order to get the best process parameters, the Taguchi method was used. By analyzing an array of experiments, it makes it possible to determine which factor is the most important, and which level of the factor is the best.

The selection of materials for metal gears is very important for improving wear resistance properties. In this study, two types of commercial metal gears, JIS-SCM415 and JIS-S45C, were used. Generally, JIS-SCM415 is used for small gears and it is a low carbon alloy steel which has a good secondary hardening effect. JIS-S45C is a low carbon steel which is commonly used to produce the gears. Both materials are widely used for transmission elements because of their relatively low cost. These gears were heat treated to increase their hardness value. The steel hardening process is essential to provide hardness, to make sure it does not wear easily when it is used. As there are a number of steel hardening methods, one of the best methods to harden only the surface is by using a laser beam. By varying the process parameters, it can produce different hardness levels at the surface.

3.1 Selection of Metal Gear Materials

In order to establish the wear mechanisms and the effect of laser processing for the materials studied, there will be wear testing of both the as received and laser treated gear materials. A series of wear tests for pitting and scuffing using a ball on disc machine will be performed with rotating and reciprocating motion respectively, using gear specimens to represent a simplified version of gear contact, i.e. line contact under high Hertzian stress between two parallel cylinders. Static contact tests will also carried out to observe the galling resistance of the surface hardened materials. An assessment of the wear damage and wear rate at each contact condition will be used to correlate the materials wear performance with their contact fatigue performance and wear simulation models in the future.

The needs for near net shape processing and improved mechanical performance are driving the use of powder metallurgy (P/M) materials for transmissions components, however these materials often perform poorly in component level rolling contact fatigue tests due to the large surface porosity and the detrimental affect this has on surface contact damage. An iron based P/M material, Ancorloy 60, has been selected as a representative of P/M materials in general given its similar composition to conventional steel, and it is anticipated that there will be a significant improvement in its wear resistance from laser surface hardening. This will allow a comparison to be made of the performance in gear contact fatigue of the P/M material against conventionally through hardened steel gears, with respect to the microstructures and wear response of the two materials.

The most commonly used carburising steel for gears is EN36, a 3% NiCrMo steel specified in British Standard 970 Part 1. The steel is through hardening and possesses a good combination of strength and toughness in the heat-treated condition, which makes it a good candidate for case hardening processing techniques such as carburising and induction hardening. However carburised gears themselves are rarely specified to be laser case hardened, and EN36 is difficult to conventionally through harden due to its hardenability and the alloy it contains. This means that the wear resistance of the gear tooth surfaces in service tends to be low due to near surface fatigue damage over time from rolling and sliding contact. The effect of this is surface pitting, with a high proportion of contact fatigue cracks and spalling.

The important issues for the choice of gear material have narrowed the choice down to two metal materials, each having certain characteristics in mechanical properties and microstructures that could affect the wear

response and hence the success of laser processing for improving their wear resistance.

3.2 Laser Surface Hardening Process Parameters

Hardness of metal gears. The parameters that affect are power, scanning speed, overlapping, spot size, and type of gas. In this research, argon gas was used as an inert gas. Spot sizes used were 1mm and 2mm. Two types of power have been chosen, low power and high power. The samples were prepared according to the international standards for abrasive wear testing, and the hardened layer was observed under a metallurgical microscope. Microhardness test data and metallography photos showed the depth and width of the hardening layer. Wear tests were conducted using pin-on-disc method. From this research, it was found that the best laser hardening results are produced using power of 1000W, scanning speed 100mm/s, argon gas, spot size 1mm, and quench method. Depth of penetration was 0.3mm with 672° microhardness value in the hardening layer and 502° on core material. Weight loss in wear testing is 10-12 mg/hr which is equivalent to the wear rate for new conventional gear. After several tests, it was concluded that the laser hardening process can increase the wear resistance of the gears. High scanning speeds and powers increased wear on the disk surface and possibly increased the temperature inside the samples, generating the thermal cracking. High scanning speeds and powers increased wear on the disk surface and possibly increased the temperature inside the samples, generating the thermal cracking.

3.3 Wear Testing Procedure

An accelerated wear testing procedure was conducted to compare the wear resistance of laser surface hardened and conventionally heat-treated gears. A modified four ball test rig was used to run the wear tests using 52100 bearing steel balls. The ball on flat configuration was chosen as it simulates a realistic gear tooth contact. The geometry of the balls was slightly modified to have a flat surface on the bottom to closely replicate the actual contact conditions. The test conditions were 294N load, 0.07m/s and the test duration was for 1 hour. This gave a total sliding distance of 252m which is sufficient to give good data repeatability. This test rig was also used in other research projects for testing gear materials. The wear volume on both the balls and discs were measured with a microbalance using Vegard's rule, with an accuracy of $1x10^{-6}mm^3$. This type of test quantifies the wear rate of the material and is good for determining the ranking of wear resistance between different materials. Further wear tests were also carried out using the same balls and disc specimens in a fully formulated gear oil under the same conditions to compare wear rates in both dry and lubricated conditions.

3.4 Data Collection and Analysis

To determine the wear volume, wear testing is carried out using a laboratory test machine known as the SRV wear testing machine. The SRV wear testing (also known as block on ring) machine is a three-order servo-hydraulic machine with a loading capacity up to 15kN. It is versatile dry and lubricated testing unit used for tribological testing of materials, lubricants and transmission elements in accordance with several national and international standard test methods. The machine can mimic actual working conditions where the gears are usually operated and can carry out wear testing for the duration required to obtain wear volume data.

Data collection is a very important step as it assists in measuring the quality of the hardened layer on the material. In this case, wear test is used to analyse the wear resistance properties of the laser surface hardened samples as compared to the samples without laser surface hardening. Wear test was conducted on the as prepared samples to obtain the initial data and also on the hardened samples after laser surface hardening is carried out on them. Wear test on the as prepared samples is carried out in order to obtain the initial wear rate and also to compare the wear rate of these samples with the samples after laser surface hardening is done on them. This will then show the difference in wear rate between the as prepared samples and the hardened samples and whether laser surface hardening will improve the

wear resistance properties of the gear samples. The wear testing results are then used to prepare graphs of wear volume against distance slid for all samples. From these graphs, the wear rate of the samples can be determined.

IV. RESULTS AND DISCUSSION

In the present work, an extensive series of pin-on-disc wear tests has been carried out using laser-treated gears in an attempt to establish the optimal conditions for wear performance in a range of gear steels. These results form the basis for assessing the wear resistance improvement achieved using laser surface hardening, the effect of process parameters on wear performance, and the wear performance of laser-treated gears compared with other surface hardening techniques. The wear tests were carried out using a block-on-ring test rig, which is designed to simulate the conditions of rolling/sliding contact experienced by gear teeth. The variation of wear rate with applied load was investigated, and the mechanism of wear established by examination of the worn surface and wear debris. In general, the wear resistance of laser-treated gears was improved considerably compared with untreated gears, and the degree of improvement was dependent on the steel and the laser hardening conditions.

Wear is one of the predominant reasons for the provision of replacement of engineering elements, and it is a very complex phenomenon involving a number of mechanisms. Laser surface hardening is a technique that improves the wear resistance of contacting surfaces by providing a thin superficial layer of high hardness. It is possible to control the microstructure and composition of the hardened layer and hence its wear properties, independently of those of the bulk material. The influence of process parameters on wear performance can also be investigated and related to the microstructural changes in the layer.

4.1 Wear Resistance Improvement in Laser Hardened Gears

Various types of surface hardening techniques, such as flame hardening, induction hardening, nitriding, and carburizing, are available to increase the surface hardness of metal. But these techniques increase the hardness of the surface up to a certain depth from the surface and also offer a hardening depth gradient. It has been reported that a higher hardness level of the gear increases the wear resistance of the gear. The depth of the hardened layer of the above-mentioned hardening processes may be sufficient to improve the wear resistance of the component, but it is very difficult to control the hardening depth, and maintaining a hardening depth gradient is dangerous for heavily loaded gears. So, it is possible that the gear may become too hard and brittle and may experience tooth breaking during operation. Therefore, it is necessary to select a hardening technique that will provide a uniform hardened layer with a controlled depth from the surface. A uniform hardened layer means constant hardness at the same depth from the surface. A very high hardness level is not required for plain carbon steel gears. A tempered gear will not be subject to brittle tooth failure. A hardened layer having a hardness of 50 to 60 HRC with a depth of 0.5 to 1 mm is cultivated for the same above-mentioned reasons. This range of hardness is quite sufficient to improve the wear resistance of the gear, and it is also possible to remove the big gear by grinding after the hardening operation in order to remove the hardened layer and any geometric changes into the tooth profile. This can be achieved if the gear is pretreated before the last hardening to remove scale and oxidation layers on the gear.

High carbon gears may be gas last hardened and directly last hardened in a protective environment can offer a surface hardened layer with controlled hardening depth, but the cost of the same is quite high. Last hardening techniques use high power density energy sources such as laser, electron beam, and plasma. High power density radiations are directed towards the material surface, and the energy of the radiation is absorbed by the material. It has been reported that by inputting an accurate quantity of heat to the material, it is possible to obtain a uniform hardened layer with controlled hardening depth. The depth of the hardened layer obtained from laser last hardening is very shallow compared to the other last hardening techniques, and it may be a suitable

last hardening process for gearing. So, last surface hardening using laser is selected as a hardening method to improve the wear resistance property of plain carbon steel gears.

In the present work, an attempt has been made to use the last surface hardening technique to improve the wear resistance properties of gears made of plain carbon steel. These gears are widely used for sugar cane crushing in the sugar industry. Such types of gears experience severe wear in field operations. The wear resistance property of the gear has been closely associated with the surface hardness of the gear. To improve wear resistance, the surface hardness of the gear should be increased and improved. It has been reported that the wear rate can be significantly reduced by increasing the surface hardness of the gear.

4.2. Effect of Process Parameters on Wear Resistance

At each of the three loads, wear rate increased with an increase in corresponding specific wear rates mentioned earlier. From these two pieces of data, wear intensity was calculated to examine the effect of pin hardness on the mated surface. Both the specific wear rate and wear intensity on the cobalt base alloy were virtually constant at all test loads. A similar situation was discovered with the heat-treated 0.5% carbon steel. Very much higher specific wear rates were encountered with the as-received steel and also the annealed steel. For the heat-treated steel, wear rate also increased with an increase in load, although it was lower than that encountered with the other forms of this alloy. This suggests that increasing gear surface hardness has a beneficial effect on wear resistance. Several changes in wear mechanism were discovered for the gear materials at various combinations of load and speed. These changes could be rationalized in terms of a modified PV value. The specific wear rate for the cobalt base alloy was almost constant at all test conditions, suggesting that abrasive wear was occurring. This is typical of adhesive wear, and the increase in wear rate with an increase in PV value is caused by the increase in surface contact temperature softening the cobalt binder phase in the cemented carbide and allowing increased adhesion to the steel counterface. This change in wear mechanism was confirmed by examining pin and tooth surfaces for evidence of transfer of cobalt base alloy.

4.3 Comparison with other Surface Hardening Techniques

Another important factor is the alloying element. The compound layer of the carburized gear tooth absorbs carbon and becomes very brittle. This is not desirable in some cases like heavy vehicle gears. An induction hardened gear absorbs less or no alloying element depending upon the material and process parameter. In this case, alloying elements do not change much and properties just alter due to a change in hardness. It quite often does not satisfy the overall aim of improving wear resistance. Laser hardening has an advantage in this case by avoiding thermal stress and surface melting the part of the gear tooth. High alloying steels can be surface melted and cooled rapidly to improve the properties without deteriorating overall properties by thermal stress.

On the other hand, the laser hardened layer has hardness more than 700 HV and the average hardness of the whole melted zone is almost equally good, which stays close to the surface hardness and gradually minimizes at a certain depth. This kind of hardness profile will ensure much better wear resistance during sliding and pitting, and it is expected that the fatigue strength of the gear tooth will also improve due to the higher hardness of the surface layer.

The properties achieved by laser hardening were compared with two conventional and most widely used surface hardening methods, i.e. gas carburizing and induction hardening. The hardness profile of the laser hardened layer is far better than the hardened case of carburizing and close to the induction hardening. The hardness profile of the carburized surface indicates a thin compound layer having hardness in the range of 900-1000 HV, which gradually minimizes and stays around 500 HV after a certain depth. The induction hardened layer has hardness more than 550 HV and gradually minimizes at greater depth.

The hardness obtained from these two techniques at the surface of the gear is not good enough to improve the wear resistance of the gear tooth during sliding to a greater extent.

V. CONCLUSION

This research has successfully demonstrated the potential of laser surface hardening (LSH) as an effective method for enhancing the wear resistance of metal gears. Through the careful selection of laser parameters, including power, scanning speed, and spot size, it was possible to achieve significant improvements in surface hardness and wear resistance. The optimized parameters resulted in a surface hardness of 672 HV and a core hardness of 502 HV for gears made of JIS-SCM415 and JIS-S45C steels. Wear testing further confirmed that the wear rate of laser-hardened gears was comparable to that of new conventional gears, with a weight loss of 10-12 mg/hr.

The study also highlighted the advantages of LSH over traditional hardening methods such as induction and flame hardening. The precision and control offered by the laser process allow for minimal distortion and the ability to target specific areas for hardening, making it particularly suitable for complex gear geometries. Furthermore, the rapid heating and cooling rates associated with LSH result in a fine microstructure that contributes to the enhanced wear resistance.

While the results are promising, it is important to note that the relationship between hardness and wear resistance is not straightforward. The wear performance of gears is influenced by a range of factors including the microstructure, residual stresses, and the presence of surface defects. Therefore, future work should focus on a deeper understanding of these factors and their interaction with the laser hardening process.

Additionally, further studies are needed to optimize the LSH process for different types of gears and materials, and to evaluate the long-term performance of laser-hardened gears in real-world applications.

In conclusion, laser surface hardening has been shown to be a viable and effective technique for improving the wear resistance of metal gears. Its ability to precisely control the hardening process and achieve desirable microstructural changes makes it a promising alternative to conventional hardening methods, with the potential to extend the service life of gears in various industrial applications.

REFERENCES

1. S. Arulvel, D. Dsilva Winfred Rufuss, A. Jain, J. Kandasamy, and M. Singhal, 'Laser processing techniques for surface property enhancement: Focus on material advancement', *Surf. Interfaces*, vol. 42, p. 103293, Nov. 2023, doi: 10.1016/j.surfin.2023.103293.
2. M. Daroonparvar *et al.*, 'Surface modification of magnesium alloys using thermal and solid-state cold spray processes: Challenges and latest progresses', *J. Magnes. Alloys*, vol. 10, no. 8, pp. 2025–2061, Aug. 2022, doi: 10.1016/j.jma.2022.07.012.
3. Y. Küçük, E. Altaş, and M. E. Topcu, 'A comparative analysis of the effect of laser surface treatment on the dry sliding wear behavior of ductile cast irons with different microstructures', *Optik*, vol. 274, p. 170540, Mar. 2023, doi: 10.1016/j.ijleo.2023.170540.
4. M. Moradi, M. Karami Moghadam, and M. Shamsborhan, 'How the laser beam energy distribution effect on laser surface transformation hardening process; Diode and Nd:YAG lasers', *Optik*, vol. 204, p. 163991, Feb. 2020, doi: 10.1016/j.ijleo.2019.163991.
5. T. Zhang, C. Zhang, L. Zhang, and J. Li, 'Evolution of thermal stress in millisecond laser manufacturing', *Opt. Commun.*, vol. 482, p. 126592, Mar. 2021, doi: 10.1016/j.optcom.2020.126592.
6. M. Moradi, S. Sharif, S. Jamshidi Nasab, and M. Karami Moghadam, 'Laser surface hardening of AISI 420 steel: Parametric evaluation, statistical modeling and optimization', *Optik*, vol. 224, p. 165666, Dec. 2020, doi: 10.1016/j.ijleo.2020.165666.
7. Y. Hu *et al.*, 'Experimental study on wear properties of wheel and rail materials with

different hardness values', *Wear*, vol. 477, p. 203831, Jul. 2021, doi: 10.1016/j.wear.2021.203831.
8. K. E. Hazzan, M. Pacella, and T. L. See, 'Laser Processing of Hard and Ultra-Hard Materials for Micro-Machining and Surface Engineering Applications', *Micromachines*, vol. 12, no. 8, p. 895, Jul. 2021, doi: 10.3390/mi12080895.
9. G. Ruiz-Ponce, M. A. Arjona, C. Hernandez, and R. Escarela-Perez, 'A Review of Magnetic Gear Technologies Used in Mechanical Power Transmission', *Energies*, vol. 16, no. 4, p. 1721, Feb. 2023, doi: 10.3390/en16041721.
10. D. J. Politis, N. J. Politis, and J. Lin, 'Review of recent developments in manufacturing lightweight multi-metal gears', *Prod. Eng.*, vol. 15, no. 2, pp. 235–262, Apr. 2021, doi: 10.1007/s11740-020-01011-5.
11. A. Rohrmoser, C. Bode, B. Schleich, H. Hagenah, S. Wartzack, and M. Merklein, 'Influence of Metal Gear Tooth Geometry on Load and Wear within Metal-Polymer Gear Pairs', *Appl. Sci.*, vol. 12, no. 1, p. 270, Dec. 2021, doi: 10.3390/app12010270.
12. N. Hou *et al.*, 'Failure modes, mechanisms and causes of shafts in mechanical equipment', *Eng. Fail. Anal.*, vol. 136, p. 106216, Jun. 2022, doi: 10.1016/j.engfailanal.2022.106216.
13. A. K. Singh, S. Kumar, B. N. Agrawal, and P. K. S. Nain, 'Design and Analysis of Spur Gear, Helical Gear, and Bevel Gear by Using ANSYS', in *Advances in Manufacturing Technology and Management*, R. M. Singari, P. K. Jain, and H. Kumar, Eds., in Lecture Notes in Mechanical Engineering. , Singapore: Springer Nature Singapore, 2023, pp. 641–650. doi: 10.1007/978-981-16-9523-0_70.
14. J. Beauson, A. Laurent, D. P. Rudolph, and J. Pagh Jensen, 'The complex end-of-life of wind turbine blades: A review of the European context', *Renew. Sustain. Energy Rev.*, vol. 155, p. 111847, Mar. 2022, doi: 10.1016/j.rser.2021.111847.
15. B. Podgornik, 'Adhesive Wear Failures', *J. Fail. Anal. Prev.*, vol. 22, no. 1, pp. 113–138, Feb. 2022, doi: 10.1007/s11668-021-01322-4.
16. N. Zhang *et al.*, 'Failure analysis of the carburized 20MnCr5 gear in fatigue working condition', *Int. J. Fatigue*, vol. 161, p. 106938, Aug. 2022, doi: 10.1016/j.ijfatigue.2022.106938.
17. W. Zhai *et al.*, 'Recent Progress on Wear-Resistant Materials: Designs, Properties, and Applications', *Adv. Sci.*, vol. 8, no. 11, p. 2003739, Jun. 2021, doi: 10.1002/advs.202003739.
18. G. Muthukumaran and P. Dinesh Babu, 'Laser transformation hardening of various steel grades using different laser types', *J. Braz. Soc. Mech. Sci. Eng.*, vol. 43, no. 2, p. 103, Feb. 2021, doi: 10.1007/s40430-021-02854-4.
19. Y. Lv, B. Cui, and Z. Sun, 'Investigation on wear behavior for SUS420 steel gear based on discrete laser surface melting', *Opt. Laser Technol.*, vol. 170, p. 110251, Mar. 2024, doi: 10.1016/j.optlastec.2023.110251.
20. E. Anusha, A. Kumar, and S. M. Shariff, 'A novel method of laser surface hardening treatment inducing different thermal processing condition for Thin-sectioned 100Cr6 steel', *Opt. Laser Technol.*, vol. 125, p. 106061, May 2020, doi: 10.1016/j.optlastec.2020.106061.
21. D. Xiang *et al.*, 'Review on wear resistance of laser cladding high-entropy alloy coatings', *J. Mater. Res. Technol.*, vol. 28, pp. 911–934, Jan. 2024, doi: 10.1016/j.jmrt.2023.11.138.

This page is intentionally left blank

Discrete Time Modeling in Hierarchically Consensus Controlled Boost based DC Micro-Grids

Miguel Parada Contzen

Bío-Bío University

ABSTRACT

This paper studies DC micro-grids in mesh topology where voltage regulation is performed at each node with help of storage devices interfaced through boost converters. Loads and distributed power sources are treated as arbitrary perturbations under a hierarchical control strategy. The primary level controller is characterized by its faster actuation rate and focus on the implementation of distributed voltage sources, while the secondary level uses a consensus algorithm to reach power sharing among the sources, and in troduces an auxiliary loop to secure voltage regulation around the nominal value. We model the entire network, considering the switching process of each individual converter, primary and secondary level controllers, hardware and communication interconnections, as a discrete time system, in opposi tion to the documented continuous time dynamic assumption. This leads to obtain an explicit representation of the entire grid, which is closer to its final hardware implementation, and facilitates dynamic trajectory analysis over specialized or conventional hardware. The developed convergence criteria for the discrete time closed loop system is corroborated by dynamic simulations which also show the main benefits of the discrete time modeling.

Keywords: dc micro grids, discrete time modeling, secondary distributed control, consensus algorithms, power sharing, mean voltage regulation.

Classification: DDC Code: 621.31

Language: English

Great Britain Journals Press

LJP Copyright ID: 392955
Print ISSN: 2631-8474
Online ISSN: 2631-8482

London Journal of Engineering Research

Volume 24 | Issue 4 | Compilation 1.0

Discrete Time Modeling in Hierarchically Consensus Controlled Boost Based DC Micro-Grids

Miguel Parada Contzen

ABSTRACT

This paper studies DC micro-grids in mesh topology where voltage regulation is performed at each node with help of storage devices interfaced through boost converters. Loads and distributed power sources are treated as arbitrary perturbations under a hierarchical control strategy. The primary level controller is characterized by its faster actuation rate and focus on the implementation of distributed voltage sources, while the secondary level uses a consensus algorithm to reach power sharing among the sources, and in troduces an auxiliary loop to secure voltage regulation around the nominal value. We model the entire network, considering the switching process of each individual converter, primary and secondary level controllers, hardware and communication interconnections, as a discrete time system, in opposi tion to the documented continuous time dynamic assumption. This leads to obtain an explicit representation of the entire grid, which is closer to its final hardware implementation, and facilitates dynamic trajectory analysis over specialized or conventional hardware. The developed convergence criteria for the discrete time closed loop system is corroborated by dynamic simulations which also show the main benefits of the discrete time modeling.

Keywords: dc micro grids, discrete time modeling, secondary distributed control, consensus algorithms, power sharing, mean voltage regulation.

Author: Electric and Electronics Department of Bío-Bío University, Chile.

I. INTRODUCTION

DC microgrids are becoming increasingly important for integrating renewable energy sources into the power grid. By utilizing distributed generation units to meet local demand, these microgrids play a critical role in the transition towards a more sustainable energy matrix [1, 2]. What started as a simple photo voltaic (PV) microgrid implementation, as seen in [3], has evolved into complex mesh topologies with distributed generation units that require autonomous control to avoid centralized planning. This approach enhances the reliability and power quality of local users [4–7].

In the context of DC microgrids with smart actuation on distributed generation units, it is possible to adopt the hierarchical control schemes proposed for AC microgrids, as presented in [6, 8, 9]. Various studies have reviewed this approach, including [10–13]. At the primary level of control, electronic power sources are implemented with commutated circuits that exhibit small time constants, which have been studied in standard power electronics textbooks such as [14, 15].

London Journal of Engineering Research

At a slower actuation rate, the secondary level of control in microgrids focuses on regulating entire microgrids with multiple active buses. Similar to multi-agent systems, each regulated voltage source must have a control unit to process signals received from other units or locally measured. This topic has been extensively documented in various sources, including books like [1, 16]. In DC microgrids, droop control is a popular strategy, as seen in [6, 17, 18]. However, consensus-based approaches have also become important in achieving global control objectives such as power sharing [19–21], voltage regulation [18, 22, 23], and more recent approaches as presented in [24–27].

While most of the literature on microgrids uses idealized continuous time dynamics, in reality, power electronic sources and distributed controllers are implemented on digital hardware that runs on different clocks. Therefore, discrete time modeling of the individual components of a microgrid is necessary for closed-loop convergence analysis, making it more applicable to the final hardware implementation. As seen in various references, such as [28–30], hardware-in-the-loop technologies and real-time simulations using dedicated hardware can be further improved with accurate modeling of the control reality, especially when hierarchical primary and secondary level controllers have different actuation rates and communication dynamics that are implemented over multiple microcontroller platforms.

In this paper, we investigate DC micro-grids with a mesh topology and bi-directional boost converters as voltage sources, controlled under primary and secondary level strategies. Our goal is to develop discrete-time models for the various components of the control plant, both individually and as a whole. This includes the power electronic switching sources, distributed primary and secondary level controllers, and the hardware and communication interconnections between them.

Drawing from existing control strategies, we focus on implementing a primary level controller that utilizes an integral action function to interface with the secondary level. The secondary level control system implements a consensus algorithm to achieve power sharing and a novel auxiliary loop to achieve voltage regulation. We present necessary conditions for control gains to guarantee convergence of the secondary level closed loop system. As a result, we present a discrete time algorithm to compute the state trajectory, taking into account the actuation rates of the different control levels and non-ideal information exchange, which can be used for the partial implementation of the system on dedicated hardware.

After this introduction, Section 2 presents the micro-grid model and its components, focusing on the discrete-time digital solution of the differential equations. In Section 3, we describe the hierarchical control strategy for digital distributed hardware and provide necessary criteria for achieving power sharing and average voltage regulation under idealized conditions. In the subsequent section, we present the computational algorithm for the closed-loop system and provide a numerical example to verify the main characteristics of the closed-loop system and the simulation methodology.

Through this paper, matrix $\mathbf{A}'$ is the transpose of $\mathbf{A}$ and $[\mathbf{A}]_{ij}$ is its element in the i-th row and the j-th column. The identity matrix and the null matrix are respectively denoted by $\mathbf{I}$ and $\mathbf{0}$. A column vector of ones is denoted as $\mathbf{1}$, and a vector with zeros in every position except in the i-th row where its value is one, is denoted as $\mathbf{s}_i \in \mathbb{R}^N$ so that $\sum_{i=1}^{N} \mathbf{s}_i = \mathbf{1}$.

II. MICRO-GRIDS IN MESH TOPOLOGY

2.1 Technological Description

Consider the two-node micro-grid illustrated in Figure 1. In this configuration, each node is equipped with a PV system, which consists of generation, conversion, and filtering stages. The PV system is designed to function as a current source, meaning that it does not regulate the voltage level at the

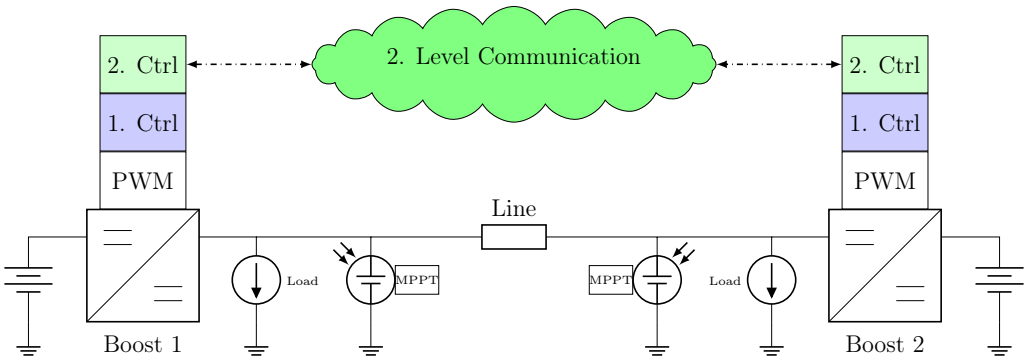

Figure 1: A two nodes example micro-grid

node. Instead, it strives to inject as much power as possible using a Maximum Power Point Tracker (MPPT) algorithm. Other types of distribution generation technologies could be modeled in a similar way. Likewise, the loads at each node can be modeled as a current source due to their unknown behavior, which may exhibit a time-variant ZIP characteristic. Since both the PV generation and load depend on unregulated external variables, they can be considered as perturbations.

To address the variability of PV generation, a storage device is connected to each node via a bidirectional DC/DC boost converter. The goal is to absorb excess power and inject it back into the system when load demand increases. These devices can be fully controlled and thus represent control actuators for voltage regulation at the nodes. Moreover, both nodes are connected to share generation and storage capacities, enabling the system to operate as a hardware-interconnected micro-grid instead of isolated nodes.

The standard approach to micro-grid control is a three-level hierarchy (e.g., [6, 8, 9]). At the primary level, the main objective is to implement individual voltage sources. This control layer can be physically implemented at each local unit without communication, relying on local measurements and actuation signals. Since the primary level plant involves fast dynamics, actuation should be performed at a high rate.

At the secondary level, control objectives are defined in terms of the entire micro-grid, rather than the individual distributed agents (i.e., the individual voltage sources serving as actuators for the secondary level process). Therefore, communication between different distributed controllers is mandatory for efficient functioning. The main goal at this level is to achieve predictable behavior of the micro-grid in terms of injected power and voltage levels, so

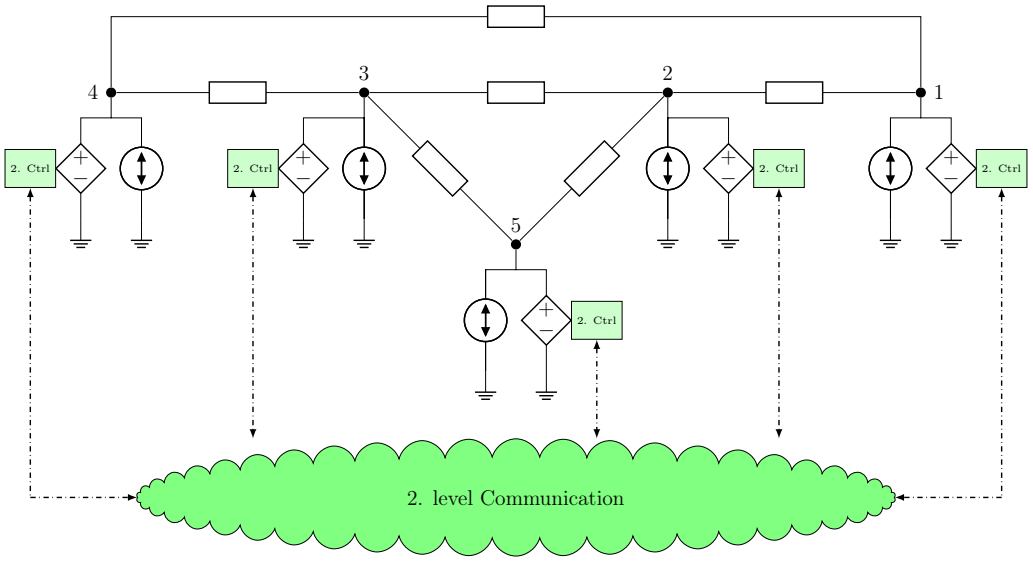

Figure 2: A five nodes example micro-grid

that the tertiary level control can rely on the fully functioning system. The higher level focuses on long-term energy exchange within the micro-grid or with respect to the main grid.

The basic idea of the two nodes micro-grid can be extended to larger system when more nodes are connected. This leads to the implementation of grids with possibly mesh-topologies as the five nodes example in Figure 2. Here, the boost converters that interface the storage devices and the primary control layer are drawn together as controllable voltage sources. The secondary layer follows the same distributed control philosophy as in the previous example. Note that the communication between the controllers is not necessarily dictated by the hardware links between the nodes. The parallel aggregation of different perturbations (loads and distributed generation) is represented by a double direction uncontrollable current source.

A micro-grid can be considered as a special case of a grid with mesh topology, in which the number of nodes, the geographical region, and the power ratings are restricted. In order to study such a reality, we need independent models of the hardware interconnections (the transmission or distribution lines) and the controllable voltage sources.

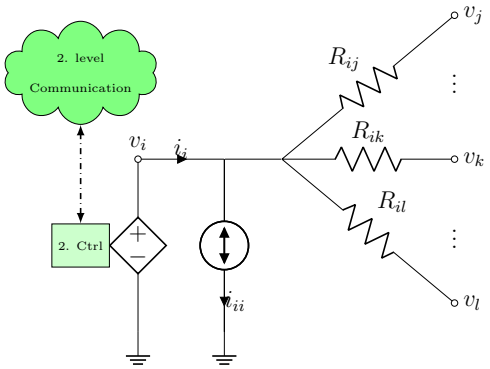

Figure 3: Voltage and current at node i of a mesh- grid with $N_i = \{j, ..., k, ..., l\}$

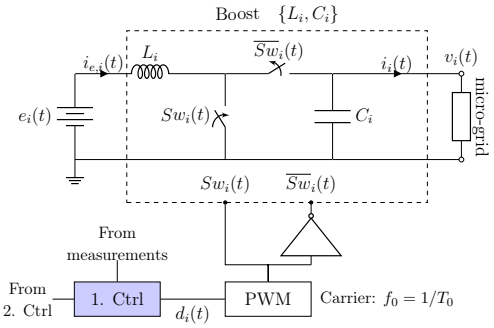

Figure 4: Ideal boost converter at the i-th node as a voltage source

2.2 Circuital Description

We will consider a mesh-grid as a graph $\mathcal{C} = (\mathcal{V}, \mathcal{E})$, with N vertices or electric nodes $i \in \mathcal{V}$, where DC voltage regulation can be performed and where loads and other generation units are connected. The undirected edges are transmission lines between the nodes, denoted $(i, j) \in \mathcal{E}$. It is assumed that the grid is connected and therefore every active node $i \in \mathcal{V}$ has at least one neighbor node $j \in \mathcal{N}_i := \{j \in \mathcal{V} | (i, j) \in \mathcal{E} \ \wedge \ i \neq j\}$.

At every active node $i \in \mathcal{V}$, we will consider that the uncontrollable current source models the aggregated behavior of all loads and distributed generators and consumes a net power $p_{ii}(t)$. In this way, if $p_{ii}(t) < 0$, the injected power at the node surpasses the power consumed by the loads. In any case, this quantity is a disturbance as it depends on external uncontrolled variables as weather or consumption.

A transmission line $(i, j) \in \mathcal{E}$ between nodes i and $j \neq i$ will be assumed as a resistance R_{ij} because the effect of inductances can be neglected in steady state. The line parameters can be estimated with reasonable accuracy due to the small size of a micro-grid. A circuital representation of a node in the grid can be seen in Figure 3.

If $i_i(t)$ is the current injected by a voltage source at node i, and $v_i(t)$ is the node voltage, from Figure 3, an expression for the current as a function of the node voltages can be obtained:

$$i_i(t) = i_{ii}(t) + \sum_{j \in \mathcal{N}_i} \frac{1}{R_{ij}} \left(v_i(t) - v_j(t) \right), \tag{1}$$

with $i_{ii}(t) = p_{ii}(t)/v_i(t)$ the net current consumed by the arbitrary loads. This expression can be generalized to all nodes by

$$\mathbf{i}_v(t) = \mathbf{i}_p(t) + \mathbf{C}\mathbf{v}(t), \tag{2}$$

where,

$$\mathbf{i}_v(t) = \operatorname{col}\left\{ i_i(t) \right\}_{i \in \mathcal{V}},$$
$$\mathbf{i}_p(t) = \operatorname{col}\left\{ i_{ii}(t) \right\}_{i \in \mathcal{V}},$$
$$\mathbf{v}(t) = \operatorname{col}\left\{ v_i(t) \right\}_{i \in \mathcal{V}},$$

and $\mathbf{C} \in \mathbb{R}^{N\times N}$ such that its elements are given $\forall i, j \in \{1, 2, ..., N\}$ by

$$[\mathbf{C}]_{ij} = \begin{cases} \sum_{k\in\mathcal{N}_i} 1/R_{ik} & \text{if } \ i = j, \\ -1/R_{ij} & \text{if } \ j \in \mathcal{N}_i, \\ 0 & \text{i.o.c.} \end{cases}$$

Because $R_{ij} = R_{ji}$, $\mathbf{C} = \hat{L}(\mathcal{C}_w)$ coincides with the Laplacian matrix, denoted $\hat{L}(\mathcal{C}_w)$, of the undirected weighted graph $\mathcal{C}_w = (\mathcal{V}, \mathcal{E}, w)$, where the weight function is given by $w((i, j)) = 1/R_{ij}$, for every edge $(i, j) \in \mathcal{E}$. It is a well known fact that $\hat{L}(\mathcal{C}_w)$ is a positive semi-definite matrix and that each row and column of $\hat{L}(\mathcal{C}_w)$ sums up to zero. *i.e.* $\hat{L}(\mathcal{C}_w)\mathbf{1} = \mathbf{0}$ and $\mathbf{1}'\hat{L}(\mathcal{C}_w) = \mathbf{0}$.

2.3 Boost Based Actuators

At every node $i \in \mathcal{V}$, an ideal bidirectional boost converter like in Figure 4 is implemented as a voltage source to regulate the tension level. The switch position, $Sw_i(t) \in \{0, 1\}$, is determined by a Pulse Width Modulation (PWM) process with a duty cycle $d_i(t) \in [0, 1]$ as input and a carrier frequency of $f_0 = {}^1/_{T_0}$.

Considering ideal switching devices, discrete states model (3) is obtained from a circuital analysis considering the cases when the switch is closed $(Sw_i(t) = 1)$, or open $(Sw_i(t) = 0)$.

$$\frac{d}{dt}\begin{bmatrix} i_{e,i}(t) \\ v_i(t) \end{bmatrix} = \begin{bmatrix} 0 & -\frac{1-Sw_i(t)}{L_i} \\ \frac{1-Sw_i(t)}{C_i} & 0 \end{bmatrix}\begin{bmatrix} i_{e,i}(t) \\ v_i(t) \end{bmatrix} + \begin{bmatrix} {}^1/_{L_i} & 0 \\ 0 & -{}^1/_{C_i} \end{bmatrix}\begin{bmatrix} e_i(t) \\ i_i(t) \end{bmatrix} \tag{3}$$

The power injected to the grid by this voltage source can be defined as

$$p_i(t) = v_i(t)i_i(t) = p_{ii}(t) + \sum_{j\in\mathcal{N}_i} \frac{v_i(t)}{R_{ij}}\left(v_i(t) - v_j(t)\right) \tag{4}$$

Note that the model of each individual voltage source depends on the current injected to the micro-grid. However, this current depends on the voltages at every node of the micro-grid. Therefore, for simulation and analysis effects, the entire micro-grid needs to be addressed as a MIMO dynamic system. By defining the following vector,

$$\mathbf{i}_e(t) = \text{col}\left\{i_{e,i}(t)\right\}_{i\in\mathcal{V}}, \quad \mathbf{x}(t) = \text{col}\left\{\mathbf{i}_e(t), \mathbf{v}(t)\right\},$$
$$\mathbf{e}(t) = \text{col}\left\{e_i(t)\right\}_{i\in\mathcal{V}}, \quad \mathbf{w}(t) = \text{col}\left\{\mathbf{e}(t), \mathbf{i}_p(t)\right\},$$

and matrices,

$$\mathbf{A}_L = \text{diag}\left\{{}^1/_{L_i}\right\}_{i\in\mathcal{V}}, \quad \mathbf{A}_C = \text{diag}\left\{{}^1/_{C_i}\right\}_{i\in\mathcal{V}},$$

$$\mathbf{S}(t) = \text{diag}\left\{Sw_i(t)\right\}_{i\in\mathcal{V}},$$

replacing equation (2), the entire system can be modeled by the linear equation (5),

$$\frac{d}{dt}\mathbf{x}(t) = \mathbf{A}(\mathbf{S}(t))\mathbf{x}(t) + \mathbf{E}\mathbf{w}(t), \tag{5}$$

where

$$\mathbf{E} = \begin{bmatrix} \mathbf{A}_L & \mathbf{0} \\ \mathbf{0} & -\mathbf{A}_C \end{bmatrix}$$

and the state matrix is a time varying function of the switches:

$$\mathbf{A}(\mathbf{S}(t)) = \begin{bmatrix} \mathbf{0} & -\mathbf{A}_L(\mathbf{I} - \mathbf{S}(t)) \\ \mathbf{A}_C(\mathbf{I} - \mathbf{S}(t)) & -\mathbf{A}_C\mathbf{C} \end{bmatrix}$$

Note that if any of the switches is closed, *i.e.* if $Sw_i(t) = 1$ for some $i \in \mathcal{V}$, an entire row of $\mathbf{A}(\mathbf{S}(t))$ is composed by zeros, and therefore it does not have an inverse.

For simulation of the system, a "real" time clock can be considered. The control actions at primary and secondary level are performed at a slower rate as this original clock. The discrete time solution of differential equation (5) can be computed under the assumptions that the perturbations and inputs are constant within the simulation discrete interval. That is, with a clock defined by $T \ll T_0$ so that $t_k = t_{k-1} + T$, if $\mathbf{w}(t) = \mathbf{w}(t_{k-1})$ and $\mathbf{S}(t) = \mathbf{S}(t_{k-1})$, $\forall t \in [t_{k-1}, t_k[$, we have that:

$$\mathbf{x}(t_k) = \mathbf{A}_d(\mathbf{S}(t_{k-1}))\mathbf{x}(t_{k-1}) + \mathbf{B}_d(\mathbf{S}(t_{k-1}))\mathbf{w}(t_{k-1}) \tag{6}$$

with discrete time matrices given by:

$$\mathbf{A}_d(\mathbf{S}(t_{k-1})) = e^{\mathbf{A}(\mathbf{S}(t_{k-1}))T}$$

$$\mathbf{B}_d(\mathbf{S}(t_{k-1})) = \left(\int_0^T e^{\mathbf{A}(\mathbf{S}(t_{k-1}))(T-\tau)} d\tau \right) \mathbf{E}$$

For a fixed $T > 0$, the previous matrices depend on the position of the switches at each instant. Therefore, there are 2^N possible values that $\mathbf{A}_d(\mathbf{S}(t_{k-1}))$ and $\mathbf{B}_d(\mathbf{S}(t_{k-1}))$ can take, which can be computed independently of time.

III. DISTRIBUTED CONTROL

3.1 Control Overview

With the equations that describe the discrete time model of the micro-grids hardware, a coherent description of the distributed control strategies is sought. Control is typically done by primary and secondary loops associated to the voltage sources. An overview of this control strategy implemented at the i-th node can be seen in the graphical representation of Figure 5. The primary level control (blue) runs over clock slower than the PWM switching process, and we will consider three sub routines. First, a feed-forward controller is defined to obtain the PWM duty cycle signal. In cascade to this, current and voltage PI loops are used to feedback all local states of the boost converter so that it can operate as a voltage source with unitary control gain.

The last part of the primary level control, implements an integral action, in such a way that the voltage source operates in the vicinity of the nominal value and the primary level input corresponds to the rate of change of the voltage deviation.

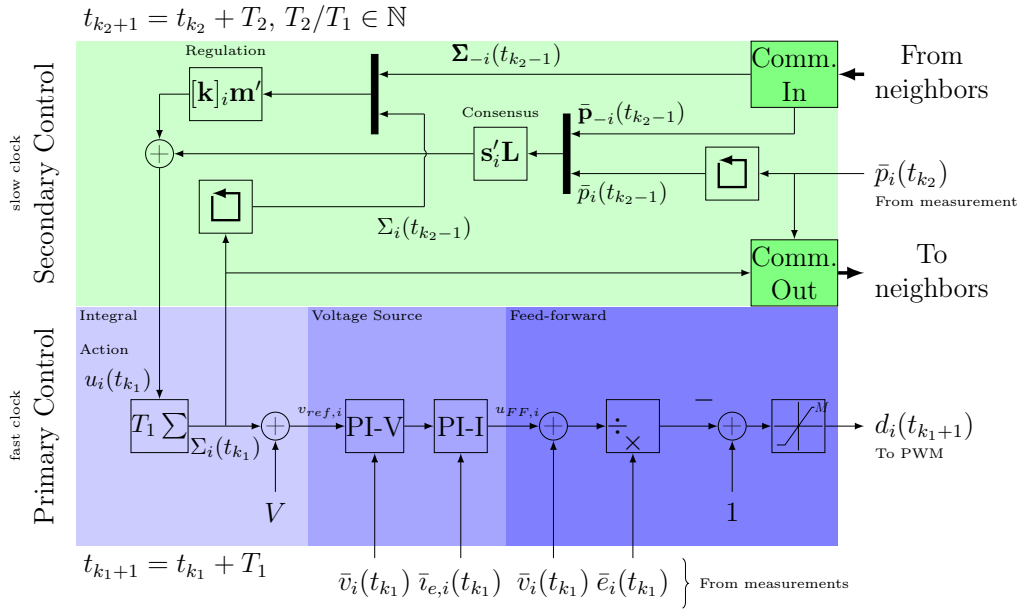

Figure 5: Distributed primary and secondary control strategy implemented at the i-th converter.

vectors concatenating the local value and the incoming signals. Note that the delay blocks are introduced in order to "wait" for the communication from the other nodes. The secondary level consist on a consensus power sharing controller with an auxiliary mean voltage regulation loop, in such a way that the voltage reference for they primary level does not deviate much from the nominal value, while the injected power by all sources is done proportionally.

We assume that the different units have independent clocks, but they are accurate enough to enforce actuation at exactly the same rate $T_1 = 1/f_1 > T_0 > T,\ \forall i \in \mathcal{V}$. We can state a counter, $k_1 \in \mathbb{N}$ on the discrete actuation instants at the primary level so that $t_{k_1} = t_{k_1-1} + T_1$. Because the secondary level dynamics are much slower than at the primary level, we can also assume that actuation is perform at a slower rate $T_2 = 1/f_2 > T_1$ and that $T_2/T_1 = n \in \mathbb{N}$. We can also state a counter, $k_2 \in \mathbb{N}$ on the discrete actuation instants at the secondary level so that $t_{k_2} = t_{k_2-1} + T_2$.

3.2. Primary Control

3.2.1 Average Measurements

In order to obtain voltage, current, and power signals for feedback, the measurement device can be considered a low pass filter with the simple transfer function

$$F_i(t) = \frac{\bar{m}_i(s)}{m_i(s)} = \frac{1}{\tau_i s + 1},$$

where $m_i(s)$ is the signal to be measured (at each node: battery voltage $e_i(t)$, capacitor voltage $v_i(t)$, inductor current $i_{e,i}(t)$, and output power $p_i(t)$) and $\bar{m}_i(s)$ its measurement after the filter. The cut-off frequency of the filter is

given by $f_{c,i} = {}^{1}/_{2\pi\tau_i}$ which can be chosen arbitrarily. The behavior of this filter at the simulation rate given by $T > 0$ can be approximated by the following differences equation

$$\bar{m}_i(t_k) = e^{-T/\tau}\bar{m}_i(t_{k-1}) + \left(1 - e^{-T/\tau}\right) m_i(t_{k-1}) \tag{7}$$

3.2.2 Feed-Forward

Following the standard argument on the mean charge and discharge times of each inductor, when ${}^{d\bar{\imath}_{e,i}}/_{dt} = 0$, we have that the static behavior between the voltages and the duty cycle at each boost satisfy

$$\bar{v}_i(t) = \frac{e_i(t)}{1 - d_i(t)}. \tag{8}$$

Solving for the duty cycle leads to propose a controller that feed-forwards the battery voltage:

$$d_i(t_{k_1+1}) = 1 - \frac{\bar{e}_i(t_{k_1})}{\bar{v}_i(t_{k_1}) + u_{FF,i}(t_{k_1})} \tag{9}$$

As the battery voltage cannot be directly manipulated, it represents a perturbation, and so this strategy can help to avoid undesired dynamics from malfunctioning batteries and it also linearizes the steady state behavior of the system.

A saturation over the value of the duty cycle can also be considered:

$$d_i(t_{k_1+1}) = \min\left\{\max\left\{d_i(t_{k_1}), d_{min}\right\}, d_{max}\right\}$$

with $d_{min} \geq 0$ and $d_{max} \leq 1$ arbitrary saturation values.

Note the intrinsic delay of the implementation of the primary controller. To assure that actuation is perform at a regular rate, the controller enforces its output at the beginning of each interval, relaying on the possible time varying computation performed in the previous interval. In this way, independently of the time needed to compute the values, the actuation over the plant is carried on at a regular basis.

As with the voltage in (8), the static relationship for the current corresponds to

$$\bar{\imath}_{e,i}(t) = \frac{\bar{\imath}_i(t)}{1 - d_i(t)}$$

Evaluating this and (8) at $t = t_{k_1+1}$ and replacing the feed-forward expression (9) leads to:

$$\bar{v}_i(t_{k_1+1}) = \frac{\bar{e}_i(t_{k_1+1})}{\bar{e}_i(t_{k_1})}\left(\bar{v}_i(t_{k_1}) + u_{FF,i}(t_{k_1})\right) \approx \bar{v}_i(t_{k_1}) + u_{FF,i}(t_{k_1})$$

$$\bar{\imath}_{e,i}i(t_{k_1+1}) = \frac{\bar{\imath}_i(t_{k_1+1})}{\bar{e}_i(t_{k_1})}\left(\bar{v}_i(t_{k_1}) + u_{FF,i}(t_{k_1})\right) \approx A\left(\bar{v}_i(t_{k_1}) + u_{FF,i}(t_{k_1})\right)$$

with approximations that hold when the perturbation signals $\bar{\imath}_i(t_{k_1})$ and $\bar{e}_i(t_{k_1})$ are constant, and $A \approx {}^{\bar{\imath}_i(t_{k_1+1})}/_{\bar{e}_i(t_{k_1})}$ constant. Because the switching process is faster than the primary controller, these equations represent an average discrete time model of the boost converter described by a states matrix with eigenvalues $\lambda_1 = 1$ and $\lambda_2 = 0$. To stabilize this system, a control law that feedbacks both states can be proposed as in the following subsection.

3.2.3 Voltage Source Implementation

The input of the feed-forward part of the controller is obtained from a control loop whose objective is to implement a voltage source with unit gain. This is typically done through a current and voltage feedback in cascade (See for example [7, 11, 12, 18, 27]). The current controller can be implemented as a discrete PI controller with the following equations:

$$\begin{aligned} e_{I,i}(t_{k_1}) &= i_{ref,i}(t_{k_1}) - \bar{\imath}_{e,i}(t_{k_1}) \\ u_{FF,i}(t_{k_1}) &= u_{FF,i}(t_{k_1-1}) + q_{0,I,i}e_{I,i}(t_{k_1}) + q_{1,I,i}e_{I,i}(t_{k_1-1}) \end{aligned} \tag{10}$$

Where the constants

$$q_{0,I,i} = K_{P,I,i} + K_{P,I,i}\frac{T_1}{2T_{I,I,i}}$$

$$q_{1,I,i} = -K_{P,I,i} + K_{P,I,i}\frac{T_1}{2T_{I,I,i}}$$

are given in terms of the proportional constant $K_{P,I,i} > 0$ and the integral time $T_{I,I,i} > 0$.

The current reference, $i_{ref,i}(t) \in \mathbb{R}$, for this loop comes from a voltage PI controller implemented by the following equations:

$$\begin{aligned} e_{V,i}(t_{k_1}) &= v_{ref,i}(t_{k_1}) - \bar{v}_i(t_{k_1}) \\ i_{ref,i}(t_{k_1}) &= i_{ref,i}(t_{k_1-1}) + q_{0,V,i}e_{V,i}(t_{k_1}) + q_{1,V,i}e_{V,i}(t_{k_1-1}) \end{aligned} \tag{11}$$

with constants

$$q_{0,V,i} = K_{P,V,i} + K_{P,V,i}\frac{T_1}{2T_{I,V,i}}$$

$$q_{1,V,i} = -K_{P,V,i} + K_{P,V,i}\frac{T_1}{2T_{I,V,i}}$$

depending on the proportional constant $K_{P,V,i} > 0$ and the integral time $T_{I,V,i} > 0$.

In this way, both states ($\bar{\imath}_{e,i}$ and $\bar{v}_i$) are used for feedback and so it is possible to achieve a unitary steady state gain between the voltage reference $v_{ref,i}(t) > 0$ and the node voltage measurement $\bar{v}_i(t) > 0$ when the controller parameters are adequately chosen.

3.2.4 Integral Action

If the input $v_{ref,i}(t) > 0$ of the voltage PI controller changes at a slow rate and within a relatively small region around the nominal value, then the boost converter can behave close to an ideal voltage source when all the control parameters are well tuned. To achieve this behavior of the reference, an integral action over the voltage deviation can be implemented with the following equations:

$$\begin{aligned} v_{ref,i}(t_{k_1}) &= \Sigma_i(t_{k_1}) + V \\ \Sigma_i(t_{k_1}) &= \Sigma_i(t_{k_1-1}) + T_1 u_i(t_{k_1}) \end{aligned} \tag{12}$$

In this way, the primary control input is the signal $u_i(t) \in \mathbb{R}$, which represents the desired change rate of the node voltage deviation from the nominal value $V > 0$; and $\Sigma_i(t) \in \mathbb{R}$ represents intern states of the primary layer.

The input to the primary level controller is determined by the secondary level at a slower rate. If a primary action instant coincides with a secondary one, that is, if $t_{k_1} = t_{k_2}$, and the speed rate between both clocks is given by $n = T_2/T_1 \in \mathbb{N}$, then there are n primary steps in every secondary step and so the previous secondary action instant coincides with the n-th previous primary instant: $t_{k_1-n} = t_{k_2-1}$.

From (12), we can write,

$$\begin{aligned} \sum_{i=0}^{n-1} \left(\Sigma_i(t_{k_1-i}) - \Sigma_i(t_{k_1-i-1})\right) &= \sum_{i=0}^{n-1} T_1 u_i(t_{k_1-i}) \\ \Sigma_i(t_{k_1}) - \Sigma_i(t_{k_1-n}) &= n T_1 u_i(t_{k_1}) \\ \Sigma_i(t_{k_2}) - \Sigma_i(t_{k_2-1}) &= T_2 u_i(t_{k_2}) \end{aligned}$$

when the input is constant $u_i(t_{k_1-i}) = u_i(t_{k_2})$, $\forall i \in \{0, \ldots, n-1\}$. That is, the integral action at the primary level can also be seen as an integral action at the secondary rate.

3.3 Secondary Control

3.3.1 Secondary Level Objectives

One common secondary level control objective is Power Sharing, or the ability of the controlled voltage sources to inject or absorb power in a predefined proportion. That is, $\forall i, j \in \mathcal{V}$,

$$\lim_{t_{k_2} \to +\infty} \frac{1}{P_i} p_i(t_{k_2}) = \lim_{t_{k_2} \to +\infty} \frac{1}{P_j} p_j(t_{k_2}) \tag{13}$$

with $P_i > 0$ a known per unification constant. The last expression defines a consensus problem and it is typically addressed with a power feedback.

As power sharing is a consensus problem, equation (13) can be written in terms of convergence to the origin of an error vector like in [31]. Consider a transformation $\mathbf{T} = D'(\mathcal{T}^o) \in \mathbb{R}^{(N-1)\times N}$ defined from an incidence matrix of a directed tree $\mathcal{T}^o = (\mathcal{V}, \mathcal{E}_T^o)$ to define an error vector

$$\mathbf{e}(t_{k_2}) := \mathbf{T}\mathbf{y}(t_{k_2}) \iff \mathbf{y}(t_{k_2}) = \mathbf{T}^{+}\mathbf{e}(t_{k_2}) + \frac{1}{N}\mathbf{1}\mathbf{1}'\mathbf{y}(t_{k_2})$$

where $\mathbf{y}(t_{k_2}) = \text{col}\left\{\frac{1}{P_i}p_i(t_{k_2})\right\}_{i\in\mathcal{V}}$ are the injected powers in per-unit, and matrix $\mathbf{T}^{+}$ is the pseudo-inverse of $\mathbf{T}$, such that $\mathbf{T}\mathbf{T}^{+} = \mathbf{I}$ and $\mathbf{T}^{+}\mathbf{T} = \mathbf{I} - \frac{1}{N}\mathbf{1}\mathbf{1}'$. It can be shown that equation (13) is equivalent to $\lim_{t_{k_2}\to+\infty}\mathbf{e}(t_{k_2}) = \mathbf{0}$.

As a result of the power sharing control strategy, the voltages at each node deviate from their nominal value, and therefore an additional objective for the entire micro-grid is voltage regulation. A linear definition of this can be stated as

$$\lim_{t_{k_2}\to+\infty}\mathbf{m}'\mathbf{v}(t_{k_2}) = V, \tag{14}$$

where the elements of $\mathbf{m}\in\mathbb{R}^N$ add up to one ($\mathbf{m}'\mathbf{1} = 1$) in such a way that $\mathbf{m}'\mathbf{v}(t_{k_2})$ represents a weighted average of the nodes voltages. Particular interesting cases are $\mathbf{m} = \frac{1}{N}\mathbf{1}$ to obtain average voltage regulation, and $\mathbf{m} = \mathbf{s}_i$ to force the i-th node to operate at nominal voltage.

We can define the per unit voltage deviation, $\Delta v_i(t_{k_2})\in\mathbb{R}$, in such a way that $v_i(t_{k_2}) = V(1+\Delta v_i(t_{k_2}))$. In vector form, $\mathbf{v}_\Delta(t_{k_2}) := \text{col}\{\Delta v_i(t_{k_2})\}_{i\in\mathcal{V}} = \frac{1}{V}\mathbf{v}(t_{k_2}) - \mathbf{1}$. If the average voltage deviation $m(t_{k_2}) := \mathbf{m}'\mathbf{v}_\Delta(t_{k_2})$ approximates the origin, then we have that

$$\lim_{t_{k_2}\to+\infty}\mathbf{m}'\mathbf{v}(t_{k_2}) = \lim_{t_{k_2}\to+\infty}V\mathbf{m}'\mathbf{v}_\Delta(t_{k_2}) + V = V$$

and voltage regulation is achieved.

3.3.2 Communication Dynamics

In order to implement any distributed secondary strategy, communication between the different agents is needed. In a realistic scenario, the model of this process needs to consider delays and information lost. Furthermore, the communication link between each node can present different dynamic and stochastic behavior. These problems can be diminish if the actuation rate of the secondary controller is slower than the expected communication time, in order to "wait" for the correct information to arrive from the neighbors. In this way, the communication process can be considered as a delay of the secondary clock.

To simulate the communication process from the j-th to the i-th agent, we consider a function of time $Comm_{ji} : \mathbb{R}^+ \mapsto \mathbb{R}^2$ in such a way that,

$$Comm_{ji}(t) = \begin{cases} \begin{bmatrix}\bar{p}_j(t-T_2)/P_j \\ \Sigma_j(t-T_2)\end{bmatrix}, \text{ if success} \\ Comm_{ji}(t-T_2), \text{ i. o. c.}\end{cases}$$

That is, the per unit power and the voltage deviation reference at the primary level of the j-th node, available for the i-th node at instant t. We consider these two variables because they will be used for the secondary level feedback in order to achieve the stated control objectives. We will consider that the communication from j to i success with a known fixed probability $[\mathbf{\Pi}]_{ji} > 0$.

With this, we can model de communication process of the entire micro-grid with help of matrices $\hat{\mathbf{P}}(t) \in \mathbb{R}^{N\times N}$ and $\hat{\mathbf{\Sigma}}(t) \in \mathbb{R}^{N\times N}$ in such a way that their elements are given by

$$\left[\hat{\mathbf{P}}(t)\right]_{ji} = \begin{cases} \bar{p}_i(t-T_2)/P_i & \text{if } \ i=j, \\ [Comm_{ji}(t)]_1 & \text{i. o. c.} \end{cases} \tag{15}$$

$$\left[\hat{\mathbf{\Sigma}}(t)\right]_{ji} = \begin{cases} \Sigma_i(t-T_2) & \text{if } \ i=j, \\ [Comm_{ji}(t)]_2 & \text{i. o. c.} \end{cases} \tag{16}$$

Note that the previous matrices consider all $N(N-1)$ possible communication channels and the N own feedback signals from each agent, independently of which channels are actually considered by the control strategy. That is, the communication problem ("*how* should information be shared?") is considered independent of the control problem ("*which* information should be shared?"). Furthermore, the communication problem is treated independently for each ordered pair (i,j) of nodes, not assuming any correlation between channels.

In the ideal case with lossless communication, all columns of the communication matrices are equal so $\hat{\mathbf{P}}(t_{k_2}) = \mathbf{y}(t_{k_2-1})\mathbf{1}'$ and $\hat{\mathbf{\Sigma}}(t_{k_2}) = \mathbf{\Sigma}(t_{k_2-1})\mathbf{1}'$ with $\mathbf{\Sigma}(t) = \text{col}\left\{\Sigma_i(t)\right\}_{i\in\mathcal{V}}$.

3.3.3 Distributed Control Strategy

Adopting the notation introduced in the previous discussion, at each node $i \in \mathcal{V}$, the secondary control action can be computed at every instant according to the following discrete time control law

$$u_i(t_{k_2}) = \mathbf{s}_i'\mathbf{L}\hat{\mathbf{P}}(t_{k_2})\mathbf{s}_i + [\mathbf{k}]_i\mathbf{m}'\hat{\mathbf{\Sigma}}(t_{k_2})\mathbf{s}_i \tag{17}$$

The feedback matrix $\mathbf{L} = -\hat{L}(\mathcal{G}_L) \in \mathbb{R}^{N\times N}$ is chosen to achieve Power Sharing similar as the strategies reviewed in, *e.g.*, [23–26, 32]. Although we consider that it is obtained as the negative Laplacian matrix of the weighted undirected graph $\mathcal{G}_L = \{\mathcal{V}, \mathcal{E}_L, w : \mathcal{E}_L \to \mathbb{R}^+\}$, it is also possible to use other matrices with the zero sum row property, $\mathbf{L1} = \mathbf{0}$. In any case, communication will be needed in every case where the off-diagonal elements of $\mathbf{L}$ are non-zero.

The vector $\mathbf{k} \in \mathbb{R}^N$, $\forall i \in \mathcal{V}$, is considered in order to achieve voltage regulation through a feedback of the voltage deviation reference, *i.e.* of the integration action at the primary level. Note that if $\mathbf{m} = \mathbf{s}_i$ and $\mathbf{k} = -K\mathbf{s}_i$ for some $K > 0$, then there is no need of communication to implement this part of the controller. As far as the authors know, this auxiliary loop has not been proposed for DC systems in other references with similar power sharing mechanisms.

With lossless communications, equation (17) can be stated for all nodes as

$$\mathbf{u}(t_{k_2}) = \operatorname{col}\left\{u_i(t_{k_2})\right\}_{i\in\mathcal{V}} = \mathbf{L}\mathbf{y}(t_{k_2-1}) + \mathbf{k}\mathbf{m}'\mathbf{\Sigma}(t_{k_2-1})$$

3.3.4 Convergence Criteria At Secondary Level

To corroborate that the discrete time implementation of the secondary level controller stabilizes the closed loop system, the following theorem gives sufficient convergence conditions for power sharing and voltage regulation under ideal conditions.

Theorem 1 (Power sharing and voltage regulation)**.** *With lossless communication, ideal voltage sources, and* $\mathbf{L}\mathbf{1} = \mathbf{0}$*, if Power Sharing and Voltage Regulation are achieved when the load of the system is constant then the eigenvalues of matrix*

$$\mathbf{A}_P = \begin{bmatrix} \mathbf{I} + VT_2\mathbf{T}\mathbf{F}\mathbf{C}\mathbf{L}\mathbf{T}^+ & V^2T_2\mathbf{T}\mathbf{F}\mathbf{C}\mathbf{k} \\ \frac{T_2}{V}\mathbf{m}'\mathbf{L}\mathbf{T}^+ & (1 + T_2\mathbf{m}'\mathbf{k}) \end{bmatrix}$$

are smaller in module than one (are within the unit circle).

Proof. If primary level controllers are properly tuned, the sources resemble ideal ones and so:

$$\mathbf{v}(t_{k_2}) \approx \operatorname{col}\left\{v_{ref,i}(t_{k_2})\right\}_{i\in\mathcal{V}} = V\mathbf{1} + \mathbf{\Sigma}(t_{k_2}).$$

In terms of the voltage deviation $\mathbf{v}_\Delta(t_{k_2}) = \frac{1}{V}\mathbf{v}(t_{k_2}) - \mathbf{1}$, the last equation can be expressed as

$$\mathbf{v}_\Delta(t_{k_2}) \approx \frac{1}{V}\mathbf{\Sigma}(t_{k_2}). \tag{18}$$

From the secondary level perspective, as the sources are assumed close to ideal, the dynamic behavior of the entire system is dictated by the integral actions in equation (12). Combining with (18) we obtain:

$$\mathbf{v}_\Delta(t_{k_2}) = \mathbf{v}_\Delta(t_{k_2-1}) + \frac{T_2}{V}\mathbf{u}(t_{k_2}) \tag{19}$$

On the other side, rearranging the voltage deviation vector as a diagonal matrix $\mathbf{V}_\Delta(t_{k_2}) = \operatorname{diag}\left\{\Delta v_i(t_{k_2})\right\}_{i\in\mathcal{V}}$ in such a way that $\mathbf{v}_\Delta(t_{k_2}) = \mathbf{V}_\Delta(t_{k_2})\mathbf{1}$, the per unit power injected by all the boost sources in equation (4) can be written in vectorial form as

$$\mathbf{y}(t_{k_2}) = \mathbf{d}(t_{k_2}) + \left(\mathbf{I} + \mathbf{V}_\Delta(t_{k_2})\right) V^2\mathbf{F}\mathbf{C}\left(\mathbf{I} + \mathbf{V}_\Delta(t_{k_2})\right)\mathbf{1} \tag{20}$$

where $\mathbf{F} = \operatorname{diag}\left\{1/P_i\right\}_{i\in\mathcal{V}}$ is a per-unification matrix and the vectors $\mathbf{y}(t_{k_2}) = \operatorname{col}\left\{p_i(t_{k_2})/P_i\right\}_{i\in\mathcal{V}}$ and $\mathbf{d}(t_{k_2}) = \operatorname{col}\left\{p_{ii}(t_{k_2})/P_i\right\}_{i\in\mathcal{V}}$ correspond respectively to the injected power by the voltage sources and the consumed power by the perturbations in per-unit.

If the voltage deviations are small (if $|\Delta v_i(t_{k_2})| \ll 1$), it makes sense to approximate the previous quadratic expression (20) by a Taylor linearization (see [26]) given by:

$$\mathbf{y}(t_{k_2}) \approx \mathbf{d}(t_{k_2}) + V^2\mathbf{FCv}_\Delta(t_{k_2}) \tag{21}$$

When the communication process introduces a unit delay but does not present information losses, the secondary level control strategy (17) can be written in terms of the consensus error and the average deviation:

$$\begin{aligned}\mathbf{u}(t_{k_2}) &= \mathbf{L}\mathbf{y}(t_{k_2-1}) + \mathbf{k}\mathbf{m}'\boldsymbol{\Sigma}(t_{k_2-1}) \\ &= \mathbf{L}\mathbf{T}^+\mathbf{e}(t_{k_2-1}) + V\mathbf{k}m(t_{k_2-1})\end{aligned}$$

when $\mathbf{L1} = \mathbf{0}$. Using this, (19), and (21), we can write for the consensus error $\mathbf{e}(t) = \mathbf{T}\mathbf{y}(t)$:

$$\begin{aligned}\mathbf{e}(t_{k_2}) - \mathbf{e}(t_{k_2-1}) &= \mathbf{T}\left(\mathbf{d}(t_{k_2}) - \mathbf{d}(t_{k_2-1})\right) + V^2\mathbf{TFC}\left(\mathbf{v}_\Delta(t_{k_2}) - \mathbf{v}_\Delta(t_{k_2-1})\right) \\ &= \mathbf{T}\Delta_1\mathbf{d}(t_{k_2}) + VT_2\mathbf{TFCu}(t_{k_2}) \\ &= \mathbf{T}\Delta_1\mathbf{d}(t_{k_2}) + VT_2\mathbf{TFCL}\mathbf{T}^+\mathbf{e}(t_{k_2-1}) + V^2T_2\mathbf{TFCk}m(t_{k_2-1})\end{aligned}$$

and for the average voltage deviation:

$$\begin{aligned}m(t_{k_2}) &= \mathbf{m}'\mathbf{v}_\Delta(t_{k_2}) \\ &= \mathbf{m}'\left(\mathbf{v}_\Delta(t_{k_2-1}) + \frac{T_2}{V}\mathbf{u}(t_{k_2})\right) \\ &= \mathbf{m}'\left(\mathbf{v}_\Delta(t_{k_2-1}) + \frac{T_2}{V}\mathbf{L}\mathbf{T}^+\mathbf{e}(t_{k_2-1}) + T_2\mathbf{k}m(t_{k_2-1})\right) \\ &= (1 + T_2\mathbf{m}'\mathbf{k})m(t_{k_2-1}) + \frac{T_2}{V}\mathbf{m}'\mathbf{L}\mathbf{T}^+\mathbf{e}(t_{k_2-1})\end{aligned}$$

Therefore, the entire linearized system can be written as:

$$\begin{bmatrix}\mathbf{e}(t_{k_2}) \\ m(t_{k_2})\end{bmatrix} = \mathbf{A}_P\begin{bmatrix}\mathbf{e}(t_{k_2-1}) \\ m(t_{k_2-1})\end{bmatrix} + \mathbf{B}_P\Delta_1\mathbf{d}(t_{k_2}) \tag{22}$$

with $\mathbf{A}_P \in \mathbb{R}^{N\times N}$ as defined before and $\mathbf{B}_P = \begin{bmatrix}\mathbf{T}' & \mathbf{0}\end{bmatrix}' \in \mathbb{R}^{N\times N}$.

From Lyapunov's first method, if the eigenvalues of $\mathbf{A}_P$ are within the unit circle, then the solution of the non-linear system at the secondary level converges. Therefore, a necessary (but not sufficient) condition for power sharing and voltage regulation with constant load (*i.e.* with $\Delta_1\mathbf{d}(t_{k_2}) = \mathbf{d}(t_{k_2}) - \mathbf{d}(t_{k_2-1}) = \mathbf{0}$), is that matrix $\mathbf{A}_P$ is Schur (has all its eigenvalues within the unit circle). □

Remark 1. Naturally, the eigenvalues of $\mathbf{A}_P$ can be used to describe the dynamic behavior of $\mathbf{e}(t_{k_2})$ and $m(t_{k_2})$. For the influence of the per unit load change, $\Delta_1\mathbf{d}(t_{k_2}) \neq \mathbf{0}$, over the consensus error, $\mathbf{e}$, robust control arguments can be used in the vicinity of the operation point. In particular, from equation (22), the $\mathtt{H}_\infty$-norm of the transfer function matrix $H_{de}(z) := \left(\mathbf{I} - z^{-1}\mathbf{A}_P\right)^{-1}\mathbf{T}$ between the load change rate and the error can be interpreted as a measurement of Power Sharing Accuracy because $\|\mathbf{e}(z)\| \leq \|H_{de}(z)\|_\infty\|\Delta_1\mathbf{d}(s)\| < +\infty$ when $\mathbf{A}_P$ is Schur.

Remark 2. Additionally, in a similar way as in [26], the non-linear equation (20) can be used to study less restrictive convergence criteria in terms of operation regions of the voltage deviations. In this way, robustness of the closed loop system against voltage changes can be characterized numerically.

Remark 3. In this way, the previous result allows to easily check for power sharing and voltage regulation, and to compare the performance of different controllers through numeric indicators. This observations can be further developed to define control design procedures. Note that when $\mathbf{m'L} = \mathbf{0}$, or when $\mathbf{Ck} = \mathbf{0}$, matrix $\mathbf{A}_P$ becomes block-triangular and its eigenvalues are dictated by the diagonal blocks.

IV. TRAJECTORY COMPUTATION

4.1 Software Implementation

Because the differential equations of the closed loop model are explicitly solved, dynamic trajectory computation of the described set-up can be efficiently implemented in any language. To do so, a basic algorithm is detailed as follow. At each instant, $t_k = t_{k-1} + T$:

1.- Choose pre-calculated matrices $\mathbf{A}_d(\mathbf{S}(t_{k-1}))$ and $\mathbf{B}_d(\mathbf{S}(t_{k-1}))$ according to the current switching configuration.

2.- Update states using equation (6).

3.- For each node $i \in \mathcal{V}$:

i) Update measurements using filters (7).

ii) If it is a secondary control instant:

- Read communicated signals.
- Update primary level input according to equation (17).

iii) If it is a primary control instant:

- Integral action in equation (12).
- Voltage PI in equation (11).
- Current PI in equation (10).
- Feed forward in equation (9).

iv) Update switching position by PWM.

v) If it is a secondary control instant:

- Update communicated signals in equations (15) and (16).

In order to obtain faster performances, the previous basic procedure can be modified to exploit specific characteristic of the chosen language, *e.g.* vectorization instead of looping; or saving variables at a slower rate. Furthermore, if $T_2/T_1 \in \mathbb{N}$ then every secondary control instant is also a primary

Table 1: Boost Sources Parameters

i	1	2	3	4	5
$L_i[mH]$	0.7417	0.7437	0.7457	0.7458	0.7513
$C_i[mF]$	4.4911	4.5264	4.4617	4.5360	4.4321
$K_{P,I,i}$			1.5		
$T_{I,I,i}$			0.01		
$K_{P,V,i}$			2.4		
$T_{I,V,i}$			0.01		
d_{min}			0.2		
d_{max}			0.8		

control instant, and so this decision does not need to be checked at every simulation instant. Further improvements can also be proposed and evaluated in any specific hardware/software configuration. However, there is no need of using specialized or tailor made solutions.

4.2 Example Micro-Grid Description

Consider the micro-grid in Figure 2 with $N = 5$ active nodes and a nominal voltage $V = 24[V]$. At each node, a boost converter is connected with nominal battery voltage $E = 12[V]$. For all nodes, the PWM process is carried out at a frequency of $f_0 = 20[kHz]$. The individual parameters of these sources are given in Table 1. All nodes are designed to inject nominal power $P_i = 50[W]$ and all measurement filters have the same time constant $\tau_i = {}^1/_{2\pi f_0}$.

The graph $\mathcal{C} = (\mathcal{V}, \mathcal{E})$ that describes the edges of the micro-grid is given in Figure 6. The resistances associated to each edge can be seen in Table 2. For all the simulations, we assume that the perturbations (battery voltage and load power) behave as in Figure 7. Note that the loads present abrupt step changes and continuously varying changes.

4.3 Primary Control Simulation

The primary control layer is implemented locally at each node, however and for simplicity, the current and voltage PI parameters are the same for every machine. These values can also be seen in Table 1. We assume that the primary actuation is performed at a rate of $T_1 = 200[\mu s]$, while the simulation step is $T = 2[\mu s]$.

Figure 6: Micro-grid graph C and consensus directed tree T^o for numeric examples

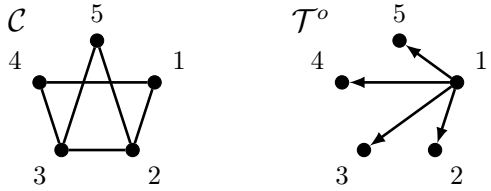

Table 2: Grid Lines Parameters. i j $R_{ij}[\Omega]$

i	j	$R_{ij}[\Omega]$
1	2	0.5044
1	4	0.4988
2	3	0.5008
3	4	0.4902
3	5	0.4936
2	5	0.5059

Figure 8 shows the behavior of the micro-grid with only the primary control layer. That is, the secondary loop action is ignored so that the voltage reference at the primary level are forced to be equal to the nominal value: $v_{ref,i}(t) = V$. Although the signals present significant ripple because of the switching process, it is clear that the voltages remain around the nominal value. Because of the feed-forward strategy, changes in the battery voltage disturb the voltage only during a brief transient. As there is no power feedback considered, the injected power by each node follows the changes of the load demand. However, the voltage is always restored to the nominal value, thus showing that the primary level implementation of the voltage sources is successful.

4.4 Secondary Control Simulation

Consider a power sharing secondary controller described by a Laplacian matrix derived from the micro-grid graph $\mathcal{C}$ in the following way:

$$\mathbf{L} = -5 \cdot \hat{L}(\mathcal{C}) = -5 \begin{bmatrix} 2 & -1 & 0 & -1 & 0 \\ -1 & 3 & -1 & 0 & -1 \\ 0 & -1 & 3 & -1 & -1 \\ -1 & 0 & -1 & 2 & 0 \\ 0 & -1 & -1 & 0 & 2 \end{bmatrix}.$$

That is, each node needs to share information only with its physical neighbors. For each edge and in both directions, we will consider that a communication link has a success probability of $[\mathbf{\Pi}]_{ij} = 0.90$, $i, j \in \mathcal{V}$. Lower success probabilities could also be considered without affecting much the overall performance. The secondary clock is given by $T_2 = 5[ms]$.

With a matrix $\mathbf{k} = \mathbf{0}$, the behavior of the micro-grid with the specified disturbances can be seen in Figure 9. Note how power sharing is achieved

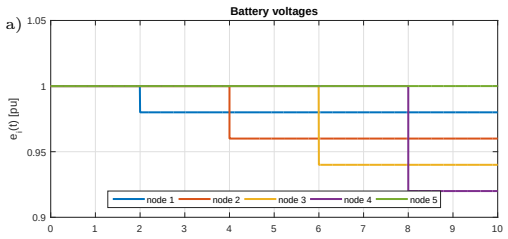

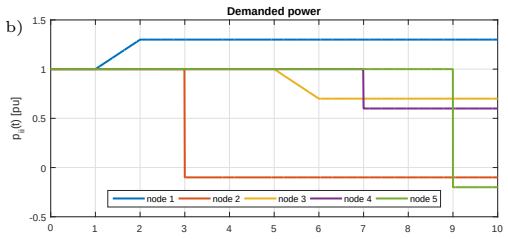

Figure 7: Perturbations for the example micro-grid. a) Battery voltage in [*p.u.*], and b) Load power consumption in [*p.u.*]

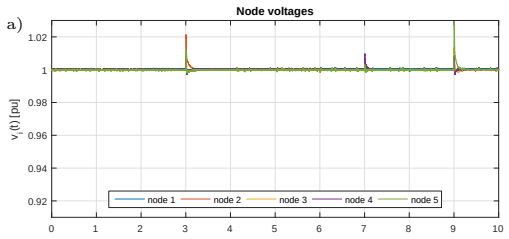

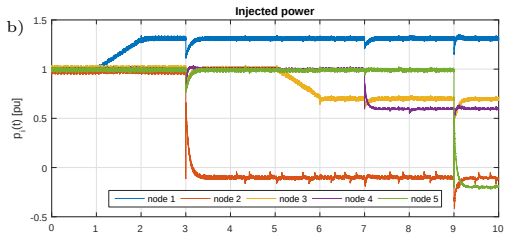

Figure 8: Behavior of micro-grid with only primary control. a) Node voltages in [*p.u.*], and b) Injected power in [*p.u.*]

within the ripple space and all the sources modify their voltages to inject power proportional to the total load. However, the voltages mean value deviates systematically from the nominal value.

To improve average voltage regulation around the nominal value, *i.e.* with $\mathbf{m} = \frac{1}{N}\mathbf{1}$, consider the matrix

$$\mathbf{k} = -2.5 \cdot \mathbf{1}.$$

Note that to implement this part of the controller all communication channels are needed. In this case, Figure 10 shows the behavior of the micro-grid. Power sharing is still achieved, but the voltages are such that their average value always is approximately the nominal value. Consequently, considering the directed tree in Figure 6, and the consensus transformation $\mathbf{T} = D'(\mathcal{T}^o) = [-\mathbf{1}, \ \mathbf{I}]$, the eigenvalues of matrix $\mathbf{A}_P$ are all contained in the unit circle satisfying the convergence criteria. In the case where $\mathbf{k} = \mathbf{0}$, the eigenvalue associated to the mean voltage deviation is identically one, and therefore this quantity cannot converge to the origin as confirmed by the simulation in Figure 9.

4.5. Comments on Simulation Speed

All previous simulations were obtained with a time step $T = 2[\mu s]$. In all cases the ratio between computation and simulation time is around ~ 8.

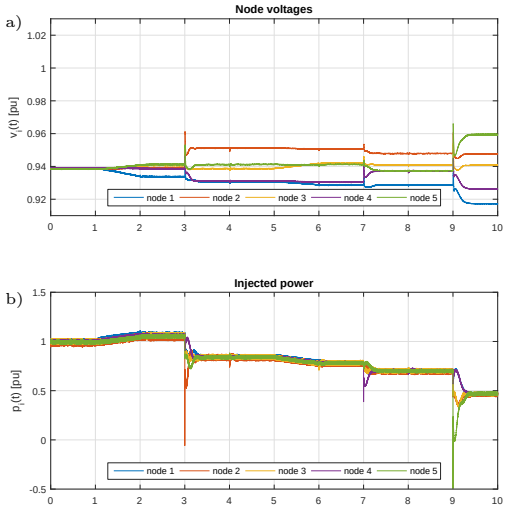

Figure 9: Behavior of micro-grid with power sharing control. a) Node voltages in [$p.u.$], and b) Injected power in [$p.u.$]

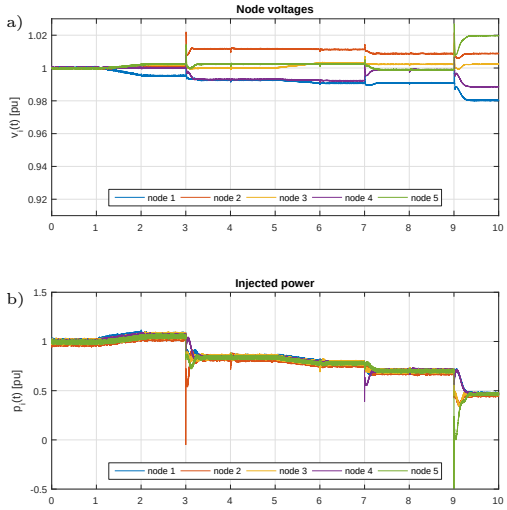

Figure 10: Behavior of micro-grid with full secondary control. a) Node voltages in [$p.u.$], and b) Injected power in [$p.u.$]

That is, to obtain the $10[s]$ shown in the graphs, around $80[s]$ were needed. Naturally, the simulation time depends on the time step used and faster simulations can be obtained by modifying this parameter. For example, Figure 11 shows the same micro-grid simulated with $T = 10[\mu s]$ and a resulting computation ratio ~ 2. This is done in a standard notebook, without any dedicated hardware or software implementation.

As is also clear from Figure 11, the speed gained by decrementing the simulation time step implies less precision. On the contrary, with $T = 0.5[\mu s]$, and a resulting ratio of ~ 35, Figure 12 shows the evolution of the system with much less numeric noise.

V. CONCLUSION

This paper focuses on DC micro-grids in mesh topology, where each node is actuated through a voltage source implemented by a storage device and a boost converter, and with loads or distributed generation units as arbitrary perturbations. We propose a general algorithm to compute the states trajectory of the closed-loop system, which considers switching devices, their hardware interconnections, a two-level control hierarchy with different actuation rates, measurement and communication dynamics, and can be used for

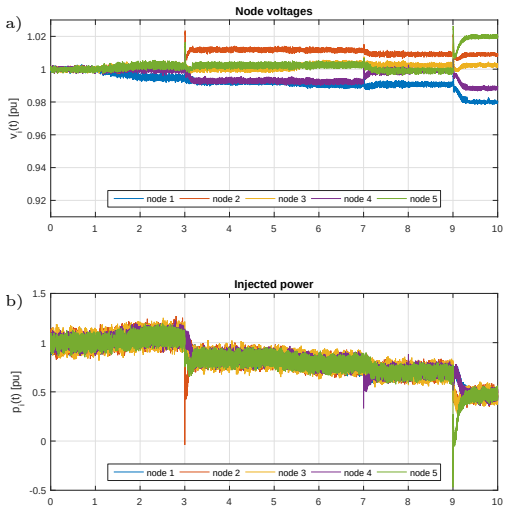

Figure 11: Behavior of micro-grid with full secondary control and $\bar{T}$ 10[μs]. a) Node voltages in [$p.u.$], and b) Injected power in [p].$u.$

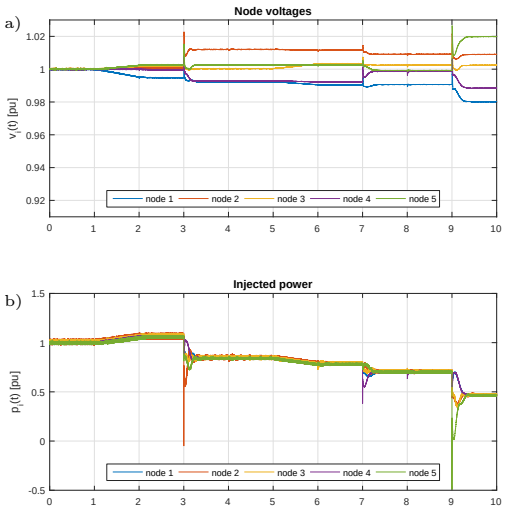

Figure 12: Behavior of micro-grid with full secondary control and T $\bar{0}$.5[μs]. a) Node voltages in [$p.u.$], and b) Injected power in [$p.u.$]

aiding implementation of hardware-in-the-loop or real-time simulations, as well as for convergence analysis.

Our primary level control includes filtered measurements, a non-linear feed-forward strategy, current and voltage PI-loops, and an integral action to actuate the switching devices as voltage sources. We present necessary conditions for convergence of the secondary level closed-loop system, which considers a consensus algorithm to achieve power sharing and a novel additional loop to reach average voltage regulation.

In contrast to idealized continuous-time dynamics, our explicit discrete-time modeling brings the convergence analysis closer to its final hardware implementation, allowing for more accurate simulation mechanisms and stability criteria. Overall, our approach provides a comprehensive solution for DC micro-grid control in mesh topology, considering the complex dynamics involved and their practical implementation.

REFERENCES

1. A. C. Zambroni de Souza, M. Castilla (Eds.), Microgrids. Design and Implementation, 1st Edition, Springer Nature Switzerland AG, 2019.
2. A. T. Elsayed, A. A. Mohamed, O. A. Mohammed, DC microgrids and distribution systems: An overview, Electric Power Systems Research 119 (2015) 407– 417.
3. H. B. H. De Zoysa, P. A. Guruge, S. R. D. Kalingamudali, N. Ku laratna, G. Kanishka, Designing and constructing a dc microgrid with uninterrupted power supply capability and optimizing its energy usage by smart controlling system, in: IEEE International Conference on In dustrial Electronics for Sustainable Energy Systems (IESES), 2018, pp. 351– 356.
4. E. Planas, J. Andreu, J. I. Gárate, Í. Martínez de Alegría, E. Ibarra, AC and DC technology in microgrids: A review, Renewable and Sustainable Energy Reviews 43 (2015) 726– 749.

5. J. J. Justo, F. Mwasilu, J. Lee, J.-W. Jung, AC-microgrids versus DC microgrids with distributed energy resources: A review, Renewable and Sustainable Energy Reviews 24 (2013) 387– 405.
6. J. M. Guerrero, J. C. Vásquez, J. Matas, L. García de Vicuña, M. Castilla, Hierarchical control of droop-controlled AC and DC micro grids – a general approach towards standarization, IEEE Transactions on Industrial Electronics 58 (2011) 158– 172.
7. Q. Shafiee, T. Dragičević, J. C. Vásquez, J. M. Guerrero, Hierarchi cal control for multiple DC-microgrids clusters, IEEE Transactions on Energy Conversion 29 (2014) 922– 933.
8. S.Peyghami, H.Mokhtari, F.Blaabjerg, Chapter 3 – Hierarchical Power Sharing Control in DC Microgrids, Vol. 1, Microgrid. Advanced Control Methods and Renewable Energy System Integration, 2017, pp. 63– 100.
9. A. Bidram, F. L. Lewis, A. Davoudi, Distributed control systems for small-scale power networks, IEEE Control Systems Magazine (2014) 56– 77.
10. F. S. Al-Ismail, DC microgrid planning, operation, and control: A com prehensive review, IEEE Access 9 (2021) 36154– 36172.
11. J. Kumar, A. Agarwal, V. Agarwal, A review on overall control of DC microgrids, Journal of Energy Storage 21 (2019) 113– 138.
12. Z. Shuai, J. Fang, F. Ning, Z. Shen, Hierarchical structure and bus volt age control of dc microgrid, Renewable and Sustainable Energy Reviews 82 (2018) 3670– 3682.
13. F. Gao, R. Kang, J. Cao, T. Yang, Primary and secondary control in dc microgrids: a review, Journal of Modern Power Systems and Clean Energy 7 (2019) 227– 242.
14. M. H. Rashid (Ed.), Power Electronics Handbook, 2nd Edition, Aca demic Press, 2007.
15. N. Mohan, T. M. Undeland, W. P. Robbins, Power Electronics. Con verters, Applications, and Design, John Wiley and Sons, 2003.
16. F. Guo, C. Wen, Y.-D. Song, Distributed Control and Optimization Technologies in Smart Grid Systems, CRC Press, 2018.
17. K. Rouzbehi, A. Miranian, J. I. Candela, Á. Luna, P. Rodríguez, A generalized voltage droop strategy for control of muliterminal DC grids, IEEE Transactions on Industry Applications 51 (2015) 607– 618.
18. N. Yang, D. Paire, F. Gao, A. Miraoui, W. Liu, Compensation of droop control using common load condition in DC microgrids to improve colt age regulation and load sharing, Electrical Power and Energy Systems 64 (2015) 752– 760.
19. M. Tucci, L. Meng, J. M. Guerrero, G. Ferrari-Trecate, Stable current sharing and voltage balancing in DC microgrids: A consensus-based secondary control layer, Automatica 95 (2018) 1– 13.
20. R. Babazadeh-Dizaji, M. Hamzeh, A. Hekmati, Power sharing in mul tiple DC microgrids based on concentrated control, in: 26th Iranian Conference on Electrica Engineering (ICEE2018), 2018, pp. 1304– 1309.
21. Y. Han, H. Li, P. Shen, E. A. Coelho, J. M. Guerrero, Review of active and reactive power sharing strategies in hierarchical controlled micro grids, IEEE Transactions on Power Electronics 32 (2017) 2427– 2451.
22. C. De Persis, E. R. Weitenberg, F. Dörfler, A power consensus algorithm for DC microgrids, Automatica 89 (2018) 364– 375.
23. B. Fan, S. Guo, J. Peng, Q. Yang, W. Liu, L. Liu, A consensus-based algorithm for power sharing and voltage regulation in DC microgrids, IEEE Transactions on Industrial Informatics 16 (2020) 3987– 3996.
24. W. Hatahet, M. I. Marei, M. Mokhtar, Adaptive controllers for grid connected DC microgrids, Electrical Power and Energy Systems 130 (2021) 106917.

25. Y. Mi, J. Guo, S. Yu, P. Cai, L. Ji, Y. Wang, D. Yue, Y. Fu, C. Jin, A power sharing strategy for islanded DC microgrid with unmatched line impedance and local load, Electric Power Systems Research 192 (2021) 106983.
26. M. Parada Contzen, Power sharing in actuated DC grids in mesh topol ogy, Sustainable Energy, Grids and Networks 28 (2021) 100523.
27. J. Lv, X. Wang, G. Wang, Y. Song, Research on control strategy of iso lated DC microgrid based on SOC of energy storage system, Electronics 10 (2021) 1– 17.
28. M. Panwar, B. Lundstrom, J. Langston, S. Suryanarayanan, S. Chakraborty, An overview of real time hardware-in-the-loop capa bilities in digital simulation for electric microgrids, in: North American Power Symposium (NAPS), 2013, pp. 1– 6.
29. M. Azeroual, T. Lamhamdi, H. E. Moussaoui, H. E. Markhi, Simulation tools for a smart grid and energy management for microgrid with wind power using multi-agent system, Wind Engineering (2019) 1–12.
30. C. Keerthisinghe, D. S. Kirschen, Real-time digital simulation of mi crogrid control strategies, in: 2020 IEEE Power and Energy Society Innovative Smart Grid Technologies Conference (ISGT), 2020, pp. 1– 5.
31. M. Parada Contzen, Consensus in networks with arbitrary time invariant linear agents, European Journal of Control 38 (2017) 52– 62.
32. J. Schiffer, T. Seel, J. Raisch, T. Sezi, Voltage stability and reactive power sharing in inverter-based microgrids with consensus-based dis tributed voltage control, IEEE Transactions on Control Systems Tech nology 24 (2016) 96–109.